

OrbView-3 Initial On-Orbit Characterization

*Kenton Ross, Vicki Zaroni, Slawomir Blonski, David Carver, Debbie Fendley, Kara Holekamp,
Mary Pagnutti, Charles Smith
John C. Stennis Space Center, Mississippi*

National Aeronautics and
Space Administration

John C. Stennis Space Center
SSC, Mississippi 39529-6000

October 2004

Acknowledgments

This work was directed by the NASA Applied Sciences Directorate (formerly the Earth Science Applications Directorate) at the John C. Stennis Space Center, Mississippi. Participation in this work by Lockheed Martin Space Operations – Stennis Programs was supported under contract number NAS 13-650. Participation in this work by Computer Sciences Corporation and by Science Systems & Applications, Inc., was supported under NASA Task Order NNS04AB54T.

Authors' Affiliations

Kenton Ross, Slawomir Blonski, Kara Holekamp, and Mary Pagnutti, Science Systems & Applications, Inc., John C. Stennis Space Center, MS (formerly with Lockheed Martin Space Operations – Stennis Programs)
Vicki Zanoni, NASA Applied Sciences Directorate, John C. Stennis Space Center, MS
David Carver, Lockheed Martin Space Operations – Diversified Programs, John C. Stennis Space Center, MS (formerly with Lockheed Martin Space Operations – Stennis Programs)
Debbie Fendley, Computer Sciences Corporation, John C. Stennis Space Center, MS (formerly with Lockheed Martin Space Operations – Stennis Programs)
Charles Smith, Lockheed Martin Integrated Systems & Solutions, Gaithersburg, MD (formerly with Lockheed Martin Space Operations – Stennis Programs)

This report contains information obtained through a Space Act Agreement among NASA John C. Stennis Space Center, Orbital Sciences Corporation, and ORBIMAGE Inc. In compliance with the terms of the Agreement, this report is being released with the permission of Orbital Sciences Corporation and ORBIMAGE Inc.

The use of trademarks or names of manufacturers is for accurate reporting only and does not constitute an official endorsement, either expressed or implied, of such products or manufacturers by the National Aeronautics and Space Administration.

Table of Contents

Executive Summary.....	viii
1.0 Introduction	1
2.0 Radiometric Characterization	2
2.1 Methodology.....	2
2.2 Results.....	3
3.0 Spatial Resolution Characterization.....	5
3.1 Methodology.....	5
3.2 Results.....	6
4.0 Geopositional Characterization	9
4.1 Methodology.....	9
4.2 Results.....	10
5.0 Summary of Results.....	11
6.0 References	11
Appendix A. Radiometry Result Plots.....	A-1
Appendix B. Edge Response Functions Measured During the Spatial Resolution Characterization .	B-1
B.1. Image ID: 14442; Acquisition Date: September 17, 2003.....	B-2
B.2. Image ID: 14442; Acquisition Date: September 17, 2003.....	B-3
B.3. Image ID: 24790; Acquisition Date: December 12, 2003.....	B-4
B.4. Image ID: 24790; Acquisition Date: December 12, 2003.....	B-5
B.5. Image ID: 22760; Acquisition Date: December 15, 2003.....	B-6
B.6. Image ID: 22760; Acquisition Date: December 15, 2003.....	B-7
B.7. Image ID: 23539; Acquisition Date: December 26, 2003.....	B-8
B.8. Image ID: 23539; Acquisition Date: December 26, 2003.....	B-9
B.9. Image ID: 24515, Acquisition Date: January 12, 2004.....	B-10
B.10. Image ID: 24515, Acquisition Date: January 12, 2004.....	B-11
Appendix C. Geopositional Accuracy Details.....	C-1
C.1. Mathematical Definitions.....	C-1
C.2. Results by Acquisition	C-3

Tables

Table 1. Radiometry acquisitions.	4
Table 2. Estimated vs. provided radiometric gain values with zero offset.	4
Table 3. Estimated radiometric gain values for September 28, 2003.	4
Table 4. Estimated radiometric gain values for October 20, 2003.	5
Table 5. OrbView-3 panchromatic images used for the spatial resolution characterization, and results of these evaluations shown as values of the Modulation Transfer Function at the Nyquist spatial frequency.	7
Table 6. Results for OrbView-3 panchromatic images used for the geopositional characterization.	10
Table C-1. Geopositional point-by-point computations, September 17, 2003.	C-3
Table C-2. Geopositional accuracy results for acquisition on September 17, 2003.	C-4
Table C-3. Geopositional point-by-point computations, December 12, 2003.	C-6
Table C-4. Geopositional accuracy results for acquisition on December 12, 2003.	C-7
Table C-5. Geopositional point-by-point computations, December 15, 2003.	C-9
Table C-6. Geopositional accuracy results for acquisition on December 15, 2003.	C-10
Table C-7. Geopositional point-by-point computations, December 26, 2003.	C-12
Table C-8. Geopositional accuracy results for acquisition on December 26, 2003.	C-13
Table C-9. Geopositional point-by-point computations, January 12, 2004.	C-15
Table C-10. Geopositional accuracy results for acquisition on January 12, 2004.	C-16

Figures

Figure 1. At-sensor radiance prediction flowchart.	3
Figure 2. Orientation and dimensions of two sets of the permanent edge targets located at the NASA Stennis Space Center in Mississippi.	5
Figure 3. An enlarged excerpt from the September 17, 2003, OrbView-3 image of an SSC edge target shows the image area extracted for the edge response analysis (C; see also Figure B-1). Measured edge responses (A) and their best fits (B) with a linear combination of three sigmoidal functions are shown as three-dimensional graphs.	7
Figure 4. LSF (A) and MTF (B) derived from the September 17, 2003, OrbView-3 image of the SSC edge targets.	8
Figure 5. Values of MTF at Nyquist frequency measured for OrbView-3 panchromatic images versus image acquisition date (A) and actual GSD (B) for the acquired image.	8
Figure 6. SSC target range geodetic targets: An individual target (A) and the overall distribution (B) overlaid on an OrbView-3 panchromatic image acquired December 15, 2003.	9
Figure 7. Spatial distribution of bias where data was orthorectified using a DEM referenced to Geodetic Reference System 1980 (GRS 80).	10
Figure A-1. Blue band composite summary result plot.	A-1

Figure A-2. Green band composite summary result plot.....	A-2
Figure A-3. Red band composite summary result plot.	A-2
Figure A-4. NIR band composite summary result plot.....	A-3
Figure A-5. Blue band individual day result plot.	A-3
Figure A-6. Green band individual day result plot.	A-4
Figure A-7. Red band individual day result plot.	A-4
Figure A-8. NIR band individual day result plot.	A-5
Figure B-1. OrbView-3 panchromatic image (<i>Georaw</i>) of the SSC edge targets and area selected for the edge response analysis in the cross-scan direction (yellow box).....	B-2
Figure B-2. OrbView-3 panchromatic image (<i>Basic</i>) of the SSC edge targets and area selected for the edge response analysis in the cross-scan direction (yellow box).....	B-2
Figure B-3. Cross-scan direction edge response extracted from the <i>Georaw</i> image.	B-2
Figure B-4. Cross-scan direction edge response extracted from the <i>Basic</i> image.	B-2
Figure B-5. OrbView-3 panchromatic image (<i>Georaw</i>) of the SSC edge targets and area selected for the edge response analysis in the along-scan direction (yellow box).	B-3
Figure B-6. OrbView-3 panchromatic image (<i>Basic</i>) of the SSC edge targets and area selected for the edge response analysis in the along-scan direction (yellow box).	B-3
Figure B-7. Along-scan direction edge response extracted from the <i>Georaw</i> image.	B-3
Figure B-8. Along-scan direction edge response extracted from the <i>Basic</i> image.	B-3
Figure B-9. OrbView-3 panchromatic image (<i>Georaw</i>) of the SSC edge targets and area selected for the edge response analysis in the cross-scan direction (yellow box).....	B-4
Figure B-10. OrbView-3 panchromatic image (<i>Basic</i>) of the SSC edge targets and area selected for the edge response analysis in the cross-scan direction (yellow box).....	B-4
Figure B-11. Cross-scan direction edge response extracted from the <i>Georaw</i> image.	B-4
Figure B-12. Cross-scan direction edge response extracted from the <i>Basic</i> image.	B-4
Figure B-13. OrbView-3 panchromatic image (<i>Georaw</i>) of the SSC edge targets and area selected for the edge response analysis in the along-scan direction (yellow box).	B-5
Figure B-14. OrbView-3 panchromatic image (<i>Basic</i>) of the SSC edge targets and area selected for the edge response analysis in the along-scan direction (yellow box).	B-5
Figure B-15. Along-scan direction edge response extracted from the <i>Georaw</i> image.	B-5
Figure B-16. Along-scan direction edge response extracted from the <i>Basic</i> image.	B-5
Figure B-17. OrbView-3 panchromatic image (<i>Georaw</i>) of the SSC edge targets and area selected for the edge response analysis in the cross-scan direction (yellow box).....	B-6
Figure B-18. OrbView-3 panchromatic image (<i>Basic</i>) of the SSC edge targets and area selected for the edge response analysis in the cross-scan direction (yellow box).....	B-6
Figure B-19. Cross-scan direction edge response extracted from the <i>Georaw</i> image.	B-6
Figure B-20. Cross-scan direction edge response extracted from the <i>Basic</i> image.	B-6
Figure B-21. OrbView-3 panchromatic image (<i>Georaw</i>) of the SSC edge targets and area selected for the edge response analysis in the along-scan direction (yellow box).	B-7
Figure B-22. OrbView-3 panchromatic image (<i>Basic</i>) of the SSC edge targets and area selected for the edge response analysis in the along-scan direction (yellow box).	B-7

Figure B-23. Along-scan direction edge response extracted from the <i>Georaw</i> image.	B-7
Figure B-24. Along-scan direction edge response extracted from the <i>Basic</i> image.	B-7
Figure B-25. OrbView-3 panchromatic image (<i>Georaw</i>) of the SSC edge targets and area selected for the edge response analysis in the cross-scan direction (yellow box).	B-8
Figure B-26. OrbView-3 panchromatic image (<i>Basic</i>) of the SSC edge targets and area selected for the edge response analysis in the cross-scan direction (yellow box).	B-8
Figure B-27. Cross-scan direction edge response extracted from the <i>Georaw</i> image.	B-8
Figure B-28. Cross-scan direction edge response extracted from the <i>Basic</i> image.	B-8
Figure B-29. OrbView-3 panchromatic image (<i>Georaw</i>) of the SSC edge targets and area selected for the edge response analysis in the along-scan direction (yellow box).	B-9
Figure B-30. OrbView-3 panchromatic image (<i>Basic</i>) of the SSC edge targets and area selected for the edge response analysis in the along-scan direction (yellow box).	B-9
Figure B-31. Along-scan direction edge response extracted from the <i>Georaw</i> image.	B-9
Figure B-32. Along-scan direction edge response extracted from the <i>Basic</i> image.	B-9
Figure B-33. OrbView-3 panchromatic image (<i>Georaw</i>) of the SSC edge targets and area selected for the edge response analysis in the cross-scan direction (yellow box).	B-10
Figure B-34. OrbView-3 panchromatic image (<i>Basic</i>) of the SSC edge targets and area selected for the edge response analysis in the cross-scan direction (yellow box).	B-10
Figure B-35. Cross-scan direction edge response extracted from the <i>Georaw</i> image.	B-10
Figure B-36. Cross-scan direction edge response extracted from the <i>Basic</i> image.	B-10
Figure B-37. OrbView-3 panchromatic image (<i>Georaw</i>) of the SSC edge targets and area selected for the edge response analysis in the along-scan direction (yellow box).	B-11
Figure B-38. OrbView-3 panchromatic image (<i>Basic</i>) of the SSC edge targets and area selected for the edge response analysis in the along-scan direction (yellow box).	B-11
Figure B-39. Along-scan direction edge response extracted from the <i>Georaw</i> image.	B-11
Figure B-40. Along-scan direction edge response extracted from the <i>Basic</i> image.	B-11
Figure C-1. Vector plot of target errors for acquisition on September 17, 2003.	C-5
Figure C-2. Vector plot of target errors for acquisition on December 12, 2003.	C-8
Figure C-3. Vector plot of target errors for acquisition on December 15, 2003.	C-11
Figure C-4. Vector plot of target errors for acquisition on December 26, 2003.	C-14
Figure C-5. Vector plot of target errors for acquisition on January 12, 2004.	C-17

Executive Summary

NASA at Stennis Space Center (SSC) established a Space Act Agreement with Orbital Sciences Corporation (OSC) and ORBIMAGE Inc. to collaborate on the characterization of the OrbView-3 system and its imagery products and to develop characterization techniques further. In accordance with the agreement, NASA performed an independent radiometric, spatial, and geopositional accuracy assessment of OrbView-3 imagery acquired before completion of the system's initial on-orbit checkout. OSC acquired OrbView-3 imagery over SSC from July 2003 through January 2004, and NASA collected ground reference information coincident with many of these acquisitions. After evaluating all acquisitions, NASA deemed two multispectral images and five panchromatic images useful for characterization. NASA then performed radiometric, spatial, and geopositional characterizations.

The multispectral images were used to assess the accuracy of the radiometric calibration. The primary targets involved were radiometric calibration tarps. Measurements of the reflectance of these tarps, as well as measurements of atmospheric conditions at the time of acquisition, were used to estimate the radiometric gain of the sensor. Because the absolute radiometric calibration coefficients provided by ORBIMAGE had zero offset, a zero offset was assumed in the gain estimate calculation. The intended result of the radiometric characterization was the deviation of calculated radiometric gain from provided radiometric gain. When the targets from both days were combined to estimate the OrbView-3 radiometric gain, the difference between the calculated and provided values ranged between approximately -1% and 7%. From the combined results, the current calibration parameters appear to be consistent with the predicted coefficients from the radiance estimation. An analysis of the measurement error for each point is being developed at SSC, but at the time of publication, was not complete. However, when the targets from each day were analyzed separately, the differences between the calculated and provided values ranged between approximately -3% and -11% for the first acquisition and between 5% and 13% for the second acquisition. The reason for this difference in results has not been determined.

The panchromatic images were used to analyze spatial resolution through edge response. The primary targets for edge response were black and white high-contrast edges painted on concrete. A region of the image containing this contrast edge was extracted and used to calculate the result. The intended result of the spatial characterization was the estimation of the Modulation Transfer Function (MTF) value at the Nyquist spatial frequency. The estimate of OrbView-3 MTF ranged between 0.05 and 0.17 for the panchromatic images with low correlation to time of acquisition. The average MTF measurements were 0.12 ± 0.04 for the Georaw images and 0.09 ± 0.04 for the Basic image products. These MTF results do not include any image sharpening processing during image reconstruction or post-processing, which represents the product delivered to the customers by default. As part of the JACIE, the sharpened products will be analyzed to determine the MTF. The panchromatic images were also used to characterize geopositional accuracy. For geopositional characterization, geodetic targets placed in an array across SSC and surveyed to high accuracy were used. The differences between the location of the target in the imagery and the known location of the target were calculated. The intended result of the geopositional characterization was an estimate of horizontal accuracy. The OrbView-3 mean Circular Error at 90% for the panchromatic images was 7.2 meters. The mean Circular Error at 95% was 7.3 meters.

1.0 Introduction

The NASA Applied Sciences Directorate (formerly the Earth Science Applications Directorate) at Stennis Space Center (SSC) serves as NASA's link to the Joint Agency Commercial Imagery Evaluation (JACIE) team, an interagency partnership between NASA, the National Geospatial-Intelligence Agency, and the U.S. Geological Survey. The JACIE team leverages each agency's expertise to characterize commercial remote sensing data purchased by the government. In this role, the Applied Sciences Directorate is responsible for the characterization and validation of commercial data used for NASA science and applications research. Characterization of commercial data is critical, because this data will potentially support science and applications that could affect global environmental policy and decision-making. The JACIE team is currently focusing its characterization efforts toward OrbView-3, a satellite built and launched by Orbital Sciences Corporation (OSC) and owned and operated by ORBIMAGE Inc. OrbView-3 acquires 4-meter multispectral (red, green, blue, and near-infrared (NIR)) and 1-meter panchromatic imagery of the Earth.

OSC is a large U.S. business and a leading manufacturer of launch vehicles and spacecraft. OSC launched the OrbView-3 satellite on June 26, 2003. ORBIMAGE is a small U.S. business and a provider of remote sensing satellite services to government and commercial customers.

NASA at SSC established a Space Act Agreement with OSC and ORBIMAGE to collaborate on the characterization of the OrbView-3 system and its imagery products and to develop characterization techniques further. Through this Space Act Agreement, OSC and ORBIMAGE will obtain an independent, initial on-orbit performance assessment of the system. By participating in this effort, the Applied Sciences Directorate helps to fulfill NASA's responsibility to characterize at least two commercial remote sensing sources/products during fiscal year 2004 as defined in the Office of Management and Budget Integrated Budget and Performance Document.

NASA scientists and others who use remote sensing data to make decisions, be they policy, economic, or scientific, should have confidence in and an understanding of the data's characteristics to make informed decisions about its use. Confidence in the data is gained by performing data characterizations or assessments. These assessments can be broken down into three categories: radiometric, spatial, and geopositional characterizations. The importance of each characterization depends on how the data will be used. Absolute radiometric characterization involves comparison between image-derived radiance values and at-sensor radiance estimates predicted by atmospheric modeling and extensive field measurements. Spatial characterization involves ground sample distance (GSD) and a measure of image sharpness, such as edge response (edge slope), line spread function, or Modulation Transfer Function (MTF). Geopositional characterization includes estimation of both horizontal and vertical accuracy of stated data coordinates. The Applied Sciences Directorate's characterization of OrbView-3 data has involved each of these three fundamental categories of remote sensing data assessment.

This initial on-orbit characterization has been accomplished using the remote sensing Verification & Validation (V&V) site developed at NASA SSC. The site, also referred to as the SSC Fee Area, is relatively square and encompasses approximately 64 sq km of Government-owned land. Land cover is predominately forested but also contains a significant number of natural and manmade features including grasslands, marshes, canals, ponds, buildings, rocket motor test stands, and roads. Targets and ground truth measurement and analysis techniques required to characterize the geometric, spatial,

and radiometric performance of a high-spatial-resolution remote sensing system have been put in place at SSC. The techniques developed at this site are examples of standardized measurement techniques (Pagnutti et al., 2002).

This document presents the methods and results of NASA's initial on-orbit radiometric, spatial, and geopositional assessment of OrbView-3 image products.

2.0 Radiometric Characterization

2.1 Methodology

Radiometric characterizations performed at SSC use a reflectance-based approach to predict at-sensor radiance. Ground-based measurements of surface target reflectance and atmospheric properties are made coincident with the satellite acquisition. For each acquisition, SSC personnel deploy up to four radiometric calibration tarps owned by SSC. Each tarp is 20 m x 20 m in size and has a relatively constant reflectance value (approximately 3.5, 22, 33, or 52%) across the visible to NIR spectral range. Additional targets used include a grass field and a concrete parking lot. Reflectance measurements are made of each target using Analytical Spectral Devices, Inc. spectroradiometers and Spectralon® reference panels that are characterized to National Institute of Standards and Technology-traceable standards. These reflectance measurements are corrected to account for the bi-directional reflectance of each target surface based on solar and satellite viewing geometries. Vertical profiles of atmospheric pressure, temperature, and humidity are collected using radiosonde weather balloons. Solar irradiance is measured with Automated Solar Radiometers and Yankee Environmental Systems Multi-Filter Rotating Shadowband Radiometers. Sky conditions and cloud cover are monitored during the data collection period using full sky imagers.

MODTRAN, the Moderate Resolution Transmittance code developed by the Air Force Research Laboratory (Berk et al., 2003), is used for radiative transport predictions. The surface and atmospheric data are used to define a radiative transport model within MODTRAN, which uses this model to propagate ground level measurements through the atmosphere to the sensor. Additional required model parameters include sensor spectral response, sensor geometry, solar geometry, and site location. The result is a prediction of at-sensor average spectral radiance per band. As a verification step before predicting at-sensor radiance, MODTRAN is run to predict the radiance of a Spectralon reference panel. The MODTRAN output radiance is compared to actual measured radiance from a reference panel at the time of overpass. This verification ensures that the defined radiative transport model is correct. A flowchart illustrating the at-sensor radiance prediction and verification process is given in [Figure 1](#).

The predicted at-sensor radiance for each target is compared to the radiance measured by the sensor. The digital numbers (DNs) of each target are obtained from each band of the image and are then area-averaged. This area-average comprises pixel DNs from the center of each target so that no edge pixels are included in the average. The number of pixels DNs averaged for each target depends on the size of the target but is typically about 9 pixels for the tarps and between 20 and 30 pixels for the grass and concrete targets. These average values are compared to the predicted at-sensor radiance for that target, and this comparison is used to estimate the gain and offset of each band. The gain and offset are calculated individually for each target. The overall estimated gain and offset for each band of the sensor is calculated using a least square fit regression line, fitted through all of the gain/offset values for each target. The uncertainty in the estimation is found using the standard deviation of the

individually calculated values. The overall estimated gain and offset are compared to those provided by the vendor to determine the accuracy of the radiometric calibration.

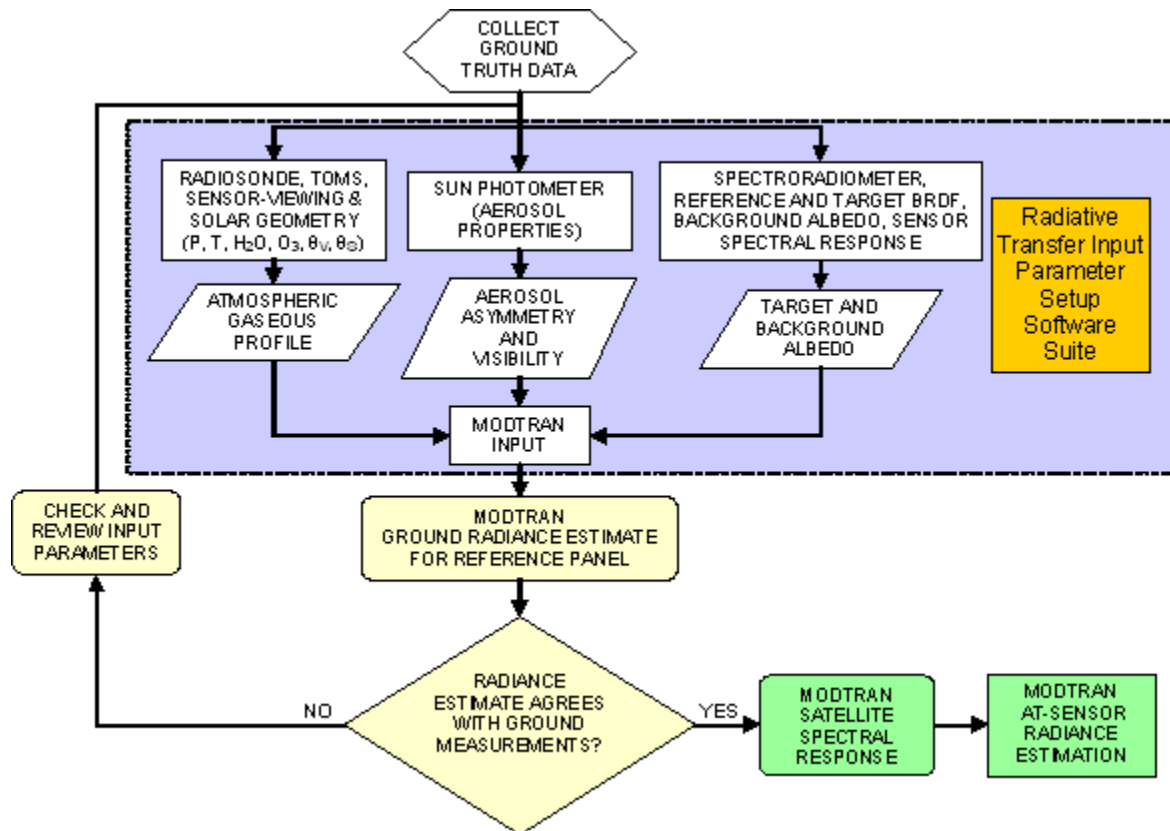


Figure 1. At-sensor radiance prediction flowchart.

2.2 Results

Two multispectral images were acquired over Stennis Space Center in the fall of 2003. The images were provided at the *Basic* product level. *Basic* images have been radiometrically corrected and include satellite telemetry data and rational functions. The two images were processed on the same day, and ORBIMAGE confirmed that the same calibration coefficients were applied to both images. Table 1 contains a list of the acquisitions, the solar and sensor viewing geometries, and the targets used.

The MODTRAN-predicted at-sensor average spectral radiance for each of the 11 targets was compared to the DN values obtained from each of the targets in the images. The relationship between the predicted radiances and the area-averaged DN values was used to estimate the overall gain of the sensor for each band using a least square fit. Because the absolute radiometric calibration coefficients provided by ORBIMAGE included a zero offset, the gain was estimated assuming a zero offset. The estimated gain was then compared to the gain provided by the vendor and percent differences between them were calculated. The uncertainty of each estimated gain was calculated using the standard deviation of the individual gain values.

Table 1. Radiometry acquisitions.

Image Archive ID	Acquisition Date	Solar Elevation	Solar Azimuth	Sensor Elevation	Sensor Azimuth	Targets
15309	9/28/2003	53.7 deg	150 deg	78.6 deg	107 deg	Tarps: 3.5%, 22%, 52% Grass; Concrete
17581	10/20/2003	46.6 deg	157 deg	74.4 deg	122 deg	Tarps: 3.5%, 22%, 34%, 52% Grass; Concrete

Table 2 contains the provided and estimated gain values, with uncertainty, the percent differences between the provided and estimated values, and the R-squared value from the least squares fit. Additionally, Figure A-1 through Figure A-4 in Appendix A contain the plots of predicted radiance versus DN values and the estimated gain value for each band.

Table 2. Estimated vs. provided radiometric gain values with zero offset.

Band	Provided Gain Value [W/(m ² sr μ m DN)]	Estimated Gain Value [W/(m ² sr μ m DN)]	Percent Difference [1 – Provided/Estimated]*100
Blue	0.26869	0.29 \pm 0.03	7.35%
Green	0.24915	0.26 \pm 0.03	4.17%
Red	0.21006	0.21 \pm 0.03	-0.03%
NIR	0.14167	0.14 \pm 0.01	-1.19%

Upon inspection of the plots, the data points from the September 28 collect fall on a line below the OrbView calibration curve, and the data points from the October 20 collect fall on a line above the curve. The OrbView calibration curve is between the points from each day, and, as a result, the difference between the provided and the average estimated gain was relatively small. Consequently, care must be taken in interpreting the low percent differences between these values in Table 2. To investigate this finding, the two days were analyzed separately. Gain values were calculated for each day. Figure A-5 through Figure A-8 in Appendix A contain plots with the new gain values. The least squares fit for each individual day shows high linear correlation; however, the composite correlation is lower as shown in Table 2. Table 3 and Table 4 contain the calculated gain values, the percent difference between the calculated values and the vendor-provided values, and the R-squared value from the least squares fit for each day. This difference between days could not be explained by any data collection or processing errors by SSC or ORBIMAGE. Additional data points are needed to evaluate this finding further.

Table 3. Estimated radiometric gain values for September 28, 2003.

Band	9/28/03 Gain Value [W/(m ² sr μ m DN)]	9/28/03 Percent Difference [1 – Provided/Estimated]*100
Blue	0.26 \pm 0.03	-3.34%
Green	0.23 \pm 0.03	-8.33%
Red	0.19 \pm 0.03	-10.56%
NIR	0.13 \pm 0.03	-8.98%

Table 4. Estimated radiometric gain values for October 20, 2003.

Band	10/20/03 Gain Value [W/(m ² sr μ m DN)]	10/20/03 Percent Difference [1 – Provided/Estimated]*100
Blue	0.31 \pm 0.01	13.33%
Green	0.28 \pm 0.02	11.02%
Red	0.23 \pm 0.02	8.67%
NIR	0.15 \pm 0.02	5.55%

3.0 Spatial Resolution Characterization

3.1 Methodology

Spatial resolution of the OrbView-3 panchromatic images was characterized by estimating value of the system MTF at the Nyquist spatial frequency. MTF values were calculated by applying the discrete Fourier transform to a Line Spread Function (LSF), which was derived from an edge response by numerical differentiation. The edge response was measured and approximated with an analytical function using a tilted-edge technique (Tzannes and Mooney, 1995). In this method, a ground-based edge target formed by adjacent black and white rectangular panels painted on a flat concrete surface is intentionally oriented so that the edge is aligned slightly off-perpendicular to a pixel grid direction on an image acquired by the tested sensor (see [Figure B-1](#) in [Appendix B](#)). Use of the tilted edge is the modification to the original knife-edge method that allows the main difficulty in applying such a method to digital images inherently based on limited, discrete spatial sampling to be overcome (Reichenbach et al., 1991). The array of permanent edge targets at SSC provides two slightly different orientations of the edges to allow for selection of the tilt angle that provides finer sampling of the edge response. Geometry and dimensions of the SSC target array are shown in [Figure 2](#).

To measure an edge response, a rectangular region containing the tilted edge is extracted from an image of the edge target as shown in [Figure B-1](#). In such a region, each line across the edge forms an approximate edge response. Exact edge responses in the direction perpendicular to the edge are obtained when distances are additionally scaled by cosine of the tilt angle. The distance correction is usually small, but it becomes important when results from measurements with different edge orientations are to be compared. To mitigate adverse effects of image noise and limited sampling, a smooth, analytical function is fitted to the edge responses. In the present approach, a superposition of three sigmoidal functions is utilized.

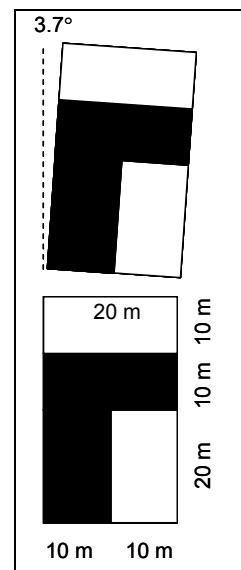


Figure 2. Orientation and dimensions of two sets of the permanent edge targets located at the NASA Stennis Space Center in Mississippi.

The fitting is performed for all the edge responses simultaneously using the following formula:

$$e_i(x) = d + \sum_{k=1}^3 \frac{a_k}{1 + \exp\left(\frac{b_1 \Delta i + b_2 - x}{c_k}\right)} \quad (1)$$

The distance x is measured in the direction perpendicular to the edge. The nonlinear least-squares optimization is conducted for nine parameters: a_1 , a_2 , a_3 , c_1 , c_2 , c_3 , b_1 , b_2 , and d . Expanding on the work of Tzannes and Mooney (1995), in the current method, position and orientation of the edge are found simultaneously, with the parameters characterizing spatial resolution, in one computational process of a nonlinear least-square fit of the two-dimensional analytical function to the intensities in the edge image (Blonski et al., 2002). The parameters a_k , b_1 , b_2 , and c_k are common for all the edge responses, while the difference in the edge position is introduced by the edge response index (i) multiplied by image GSD (Δ). Because all of the edge positions are located on a straight line, they are specified with the simple formula $b_1 \Delta i + b_2$. Tangent of the tilt angle is equal to the absolute value of the parameter b_1 . To suppress noise artifacts further, all three sigmoidal functions are restricted to the same positions of the edge specified by the parameters b_1 and b_2 . This assumption also ensures that the analytical edge response function is symmetrical. Finding the parameters b_1 and b_2 during the curve-fitting process is equivalent to shifting the edge responses to a single reference location so that all the edge points are aligned. Superimposing all the shifted edge responses creates a new edge response with a finer spatial sampling.

After an analytical edge response function is obtained from the best fit, the function is differentiated numerically to derive an LSF. The LSF is then Fourier transformed to generate an MTF for a range of spatial frequencies up to the sampling frequency. Value of MTF at the Nyquist frequency (half the sampling frequency) is subsequently extracted to provide the final result of the spatial resolution characterization.

3.2 Results

Five panchromatic images acquired by the OrbView-3 satellite over the Stennis Space Center area were used in the spatial resolution characterization (see [Table 5](#)). Because each image was provided at two processing levels: *Georaw* and *Basic*,¹ 10 OrbView-3 image products were available for the analysis. For each of the 10 image products, spatial resolution was evaluated in two perpendicular directions, cross-scan and along-scan, in relation to the scanning direction of the OrbView-3 pushbroom camera. Results of these evaluations are shown in [Table 5](#).

Edge responses extracted from the OrbView-3 panchromatic images of the SSC edge targets are presented on graphs included in [Appendix B](#). Analytical functions fitted to the edge response data points are shown in those figures as well.

¹ The *Georaw* version is an intermediate image in the ground processing chain where the individual detectors on the focal plane are aligned by a nominal 4-pixel shift in the along-scan direction to adjust for the staggered layout of the panchromatic detectors along the focal plane array. The *Georaw* version is engineering data that best describes the camera MTF without the effects of ground processing required for product generation. The *Georaw* version is not a product that is delivered to customers. The *Basic* product includes a cubic interpolation to align the detectors better along the focal plane and to correct for sensor artifacts such as smile and attitude smoothing. This product retains satellite geometry; that is, no rectification has been performed.

Table 5. OrbView-3 panchromatic images used for the spatial resolution characterization, and results of these evaluations shown as values of the Modulation Transfer Function at the Nyquist spatial frequency.

Image Archive ID	Acquisition Date	Satellite Angle [°]		GSD [m]		MTF at Nyquist frequency			
		Zenith	Azimuth	Cross-scan	Along-scan	Cross-scan (Georaw)	Cross-scan (Basic)	Along-scan (Georaw)	Along-scan (Basic)
14442	09/17/03	10.7	84.5	1.02	0.99	0.16	0.15	0.14	0.08
24790	12/12/03	24.2	100.0	1.18	1.08	0.15	0.05	0.16	0.17
22760	12/15/03	37.3	91.9	1.54	1.21	0.09	0.05	0.13	0.08
23539	12/26/03	9.8	98.4	1.02	0.99	0.11	0.06	0.16	0.15
24515	01/12/04	28.4	87.1	1.26	1.10	0.07	0.08	0.08	0.09

Examples of the measured edge responses and their fitted analytical functions are shown on three-dimensional graphs in [Figure 3](#). These graphs show the shifted edge response functions before they are superimposed. An excerpt from the original image displays the set of pixels used in the extraction of the edge responses.

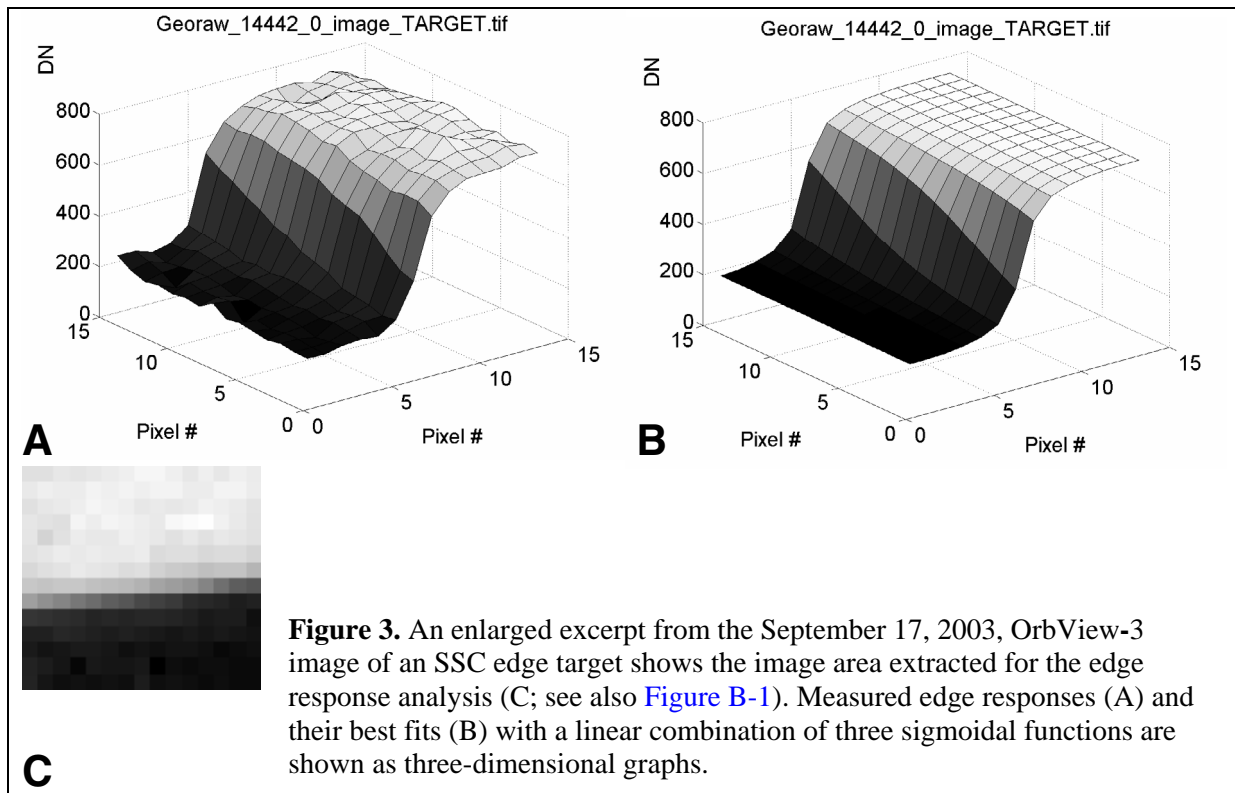


[Figure 4](#) presents examples of Line Spread Function and Modulation Transfer Function derived from the analytical function fitted to an OrbView-3 edge response function. Value of MTF at the Nyquist frequency is also indicated in this figure.

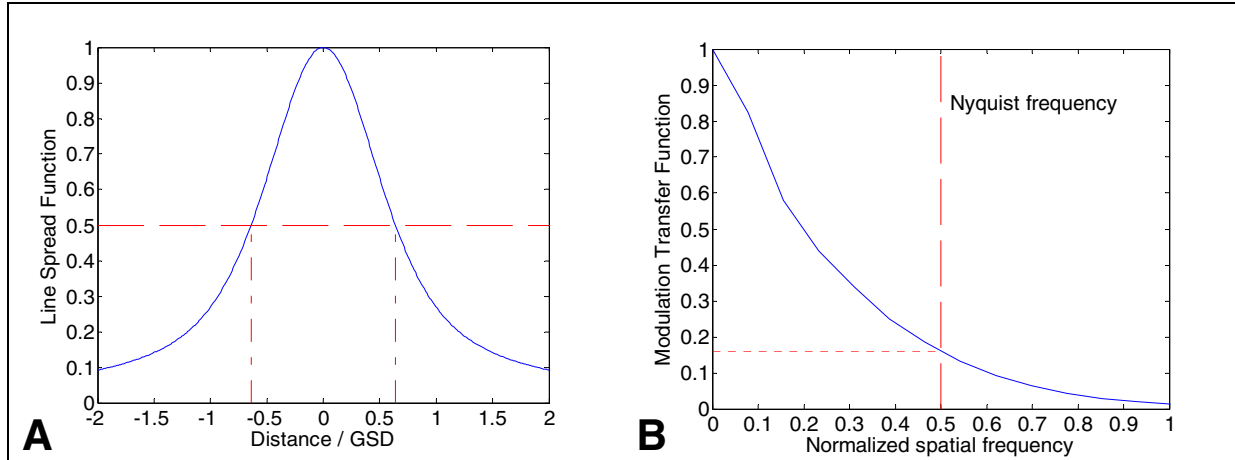


Figure 4. LSF (A) and MTF (B) derived from the September 17, 2003, OrbView-3 image of the SSC edge targets.

Numerical data from Table 5 are plotted in Figure 5 versus date of image acquisition and actual GSD, which is determined by the acquisition geometry (satellite azimuth and zenith angles). The measured values of MTF at Nyquist frequency are in the range from 0.05 to 0.17. In most cases, the MTF values are higher for the *Georaw* images than for the *Basic* images from the same acquisition. Figure 5 shows that there is no clear indication of any correlation between time of acquisition and spatial resolution of the OrbView-3 images. ORBIMAGE has confirmed that no changes to sensor settings (e.g., focus) were made during the time period of these acquisitions. As expected, the observed correlation between MTF at Nyquist frequency and acquisition GSD is not very strong. Therefore, the differences between the results were interpreted as random errors, and mean values and standard deviations of the MTF at Nyquist frequency were calculated. The average MTF measurement results are 0.12 ± 0.04 for the *Georaw* images and 0.09 ± 0.04 for the *Basic* image products with the geometric mean applied to combine results for the cross-scan and along-scan directions. No sharpening was applied to this imagery during product generation.

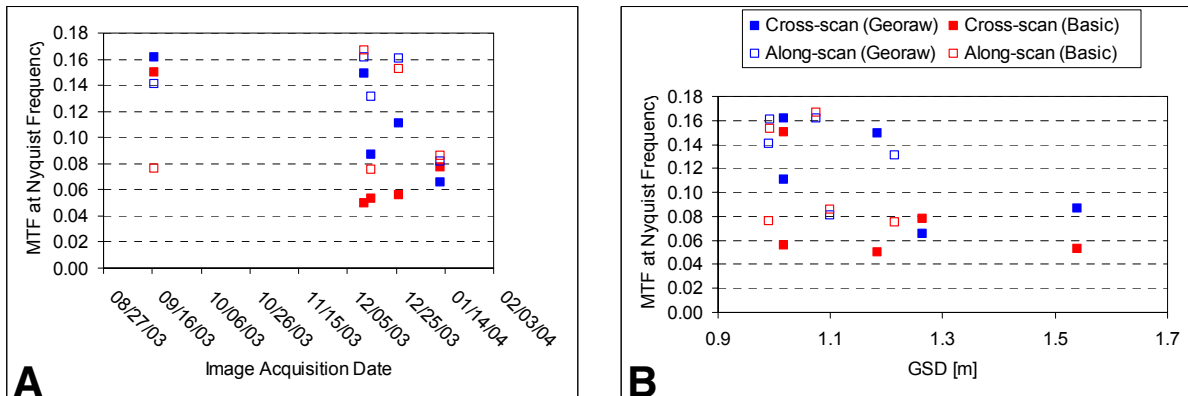


Figure 5. Values of MTF at Nyquist frequency measured for OrbView-3 panchromatic images versus image acquisition date (A) and actual GSD (B) for the acquired image.

4.0 Geopositional Characterization

4.1 Methodology

The SSC V&V site includes an array of 45 manmade geodetic targets. The targets, which are distributed uniformly throughout the SSC Fee Area, are circular, 2.44m in diameter, and painted white with a 0.6-m diameter center that is painted red (Figure 6). Target centers have been geolocated by Global Positioning System (GPS) technology to within 3-cm horizontal and 6-cm vertical accuracy.

The OrbView-3 imagery was first assessed to determine how many geodetic targets could be unambiguously located. As specified in the National Standard for Spatial Data Accuracy (NSSDA) (FGDC, 1998), a minimum of 20 points must be tested to determine positional accuracy. Where 20 or more targets were clearly visible, the imagery was then orthorectified to reduce terrain effects. The orthorectification was carried out using a rational polynomial coefficient model supplied with the imagery and a digital elevation model (DEM) of the SSC Fee

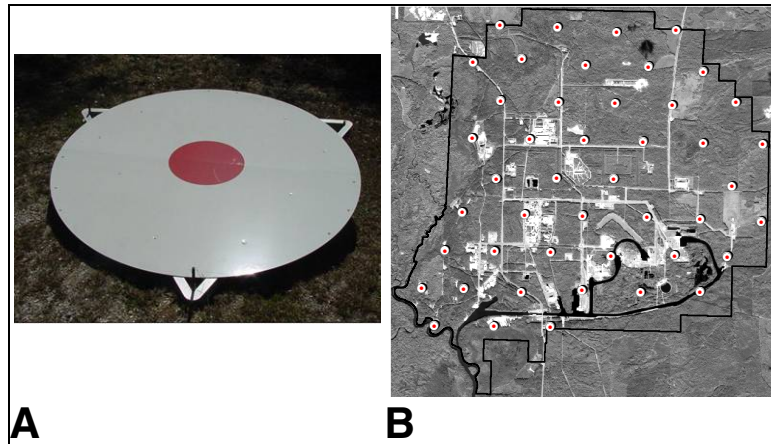


Figure 6. SSC target range geodetic targets: An individual target (A) and the overall distribution (B) overlaid on an OrbView-3 panchromatic image acquired December 15, 2003.

Area produced by photogrammetric methods using aerial imagery. The accuracy of the DEM has been estimated by spot checks to be 0.8 m vertically and 0.5 m horizontally. The DEM was originally referenced to an orthometric datum (North American Vertical Datum 1988) but was converted to an ellipsoidal datum (Geodetic Reference System 1980) using GEOID03, the current model of the geoid from the National Geodetic Survey at the time this report was generated.

Using the orthorectified imagery, the geodetic target locations were compared with the known (GPS-surveyed) locations of the geodetic targets. For each location, the differences in Northing (y component) and Easting (x component) were calculated. Based on these differences, or deltas, at each target, a series of intermediate statistics was computed: the bias (mean error), the estimated random error (standard deviation of the deltas after removing the bias), the ratio of bias to random error, and the ratio of minimum to maximum in the x and y components of random error (an indicator of how close the error distribution is to circular). From these computations, additional statistics were generated, including Root Mean Squared Error (RMSE) and Circular Error at the 90% (CE_{90}) and 95% (CE_{95}) levels. Mathematical descriptions of the statistics used in this characterization are listed in [Appendix C](#).

4.2 Results

Overall, the mean CE_{90} of OrbView-3 panchromatic images characterized was 7.2 m and the mean CE_{95} was 7.3 m. Assuming a normal distribution, a 95% confidence interval for the CE_{90} of the OrbView-3 system was estimated with a lower bound of 4.0 m and an upper bound of 10.3 m, and a 95% confidence interval for the CE_{95} was estimated with a lower bound of 4.1 m and an upper bound of 10.4 m. With only 4 degrees of freedom, this result is preliminary. The geopositional results by acquisition are shown in [Table 6](#).

Table 6. Results for OrbView-3 panchromatic images used for the geopositional characterization.

Archive ID	Acquisition Date	Bias X	Bias Y	μ_H (Bias)	σ_c (Circular Standard Error)	CE_{90}	CE_{95}
14442	09/17/03	-5.88	-5.31	7.92	0.64	8.29	8.37
24790	12/12/03	-4.46	1.45	4.69	0.50	5.49	5.66
22760	12/15/03	-1.21	-9.73	9.80	1.00	11.11	11.19
23539	12/26/03	2.11	-3.84	4.38	0.53	4.98	5.13
24515	01/12/04	-5.21	-1.48	5.42	0.48	5.92	5.96

The presence of a bias in the data that is roughly a factor of 10 greater than estimated random error is consistent with an error model where the most significant source of error is sensor pointing error. The proportion of bias to random error was stable through all five acquisitions. However, there was no clear pattern in the direction of the bias as shown in [Figure 7](#). Further detail, including complete point-by-point calculations and vector plots, is included in [Appendix C](#).

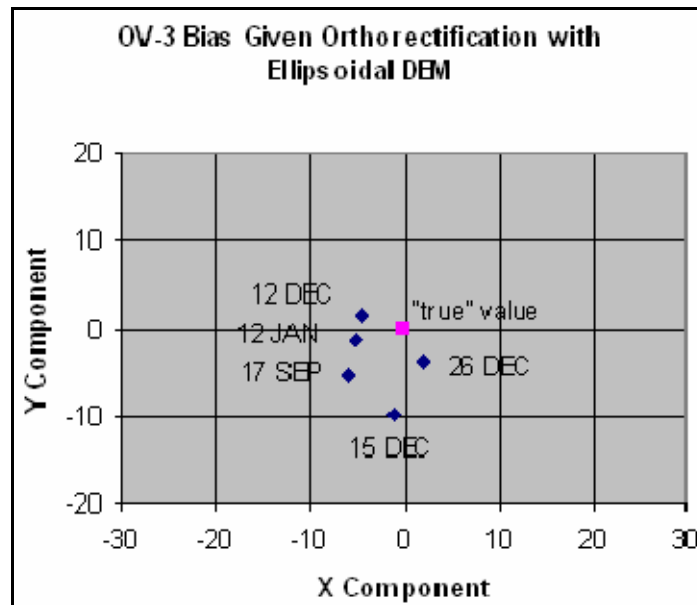


Figure 7. Spatial distribution of bias where data was orthorectified using a DEM referenced to Geodetic Reference System 1980 (GRS 80).

5.0 Summary of Results

The NASA initial on-orbit characterization of OrbView-3 imagery produced the following results:

1. Radiometric characterization determined that the estimated gain coefficients deviated little from the provided gain coefficients. In the worst case, the blue band deviation was slightly greater than 7%. In the red band, the estimated gain deviated less than 0.05% from the provided gain. However, when the two multispectral acquisitions were considered separately, larger variation was observed. This outcome, however, is the result of having only two acquisitions to use in the analysis. The cause of the variability between these two days has not been identified and will be studied further using additional acquisitions collected over the coming year.
2. Average MTF values at Nyquist spatial frequency for five panchromatic acquisitions are 0.12 ± 0.04 for the *Georaw* images and 0.09 ± 0.04 for the *Basic* image products. These MTF results do not include any image sharpening processing during image reconstruction or post-processing, which represents the product delivered to the customers by default.
3. Geopositional error resulting from provided rational polynomial coefficient models for five panchromatic images ranged from 5.1 m to 11.2 m (CE_{95} computed empirically). The error for each image was dominated by a single displacement or “bias” with bias to random error ratio approximately 10:1. There was no clear trend in the direction of the bias.

The JACIE team will perform additional independent characterization of OrbView-3 image products in the coming months. Further radiometric, spatial, and geopositional assessments will be conducted over a longer time period with additional data acquisitions and sites.

6.0 References

- Ager, T.P., 2004. *An Analysis of Metric Accuracy Definitions and Methods of Computation*. White paper written for NIMA InnoVision.
- Berk, A., G.P. Anderson, P.K. Acharya, M.L. Hoke, J.H. Chetwynd, L.S. Bernstein, E.P. Shettle, M.W. Matthew, and S.M. Adler-Golden, 2003. *MODTRAN4 Version 3 Revision 1 User's Manual*. Air Force Research Laboratory, Space Vehicles Directorate, Air Force Materiel Command, Hanscom AFB, Massachusetts.
- Blonski, S., M. Pagnutti, R.E. Ryan, and V. Zanoni, 2002. In-flight edge response measurements for high-spatial-resolution remote sensing systems. In: *Earth Observing Systems VII*, W.L. Barnes, Editor, *Proceedings of SPIE*, 4814:317–326.
- Federal Geographic Data Committee, 1998. *Geospatial Positioning Accuracy Standards Part 3: National Standard for Spatial Data Accuracy*. FGDC-STD-007.3-1998, Federal Geodetic Data Committee, Washington D.C., 25 pp.
- Greenwalt, C.R., and M.E. Schultz, 1962. *Principles of Error Theory and Cartographic Applications*. ACIC Technical Report No. 96, United States Air Force, Aeronautical Chart and Information Center, St. Louis, Missouri, 98 pp.
- Pagnutti, M., K. Holekamp, R. Ryan, S. Blonski, R. Sellers, B. Davis, and V. Zanoni, 2002. Measurement sets and sites commonly used for characterization. *Proceedings of ISPRS*

Commission I Symposium, Integrated Remote Sensing at the Global, Regional and Local Scale, November 10–15, Denver, CO, (IAPRS, Vol. XXXIV, part 1), http://www.isprs.org/commission1/proceedings/paper/MPagnutti_ISPRS2002.pdf (last accessed 09/23/04).

Reichenbach, S. E., S.K. Park, and R. Narayanswamy, 1991. Characterizing digital image acquisition devices. *Optical Engineering*, 30(2):170–177.

Tzannes, A.P., and J.M. Mooney, 1995. Measurement of the modulation transfer function of infrared cameras. *Optical Engineering*, 34(6):1808–1817.

U.S. Bureau of the Budget, 1947. *United States National Map Accuracy Standards*. Office of Management and Budget, Washington, D.C.

Appendix A. Radiometry Result Plots

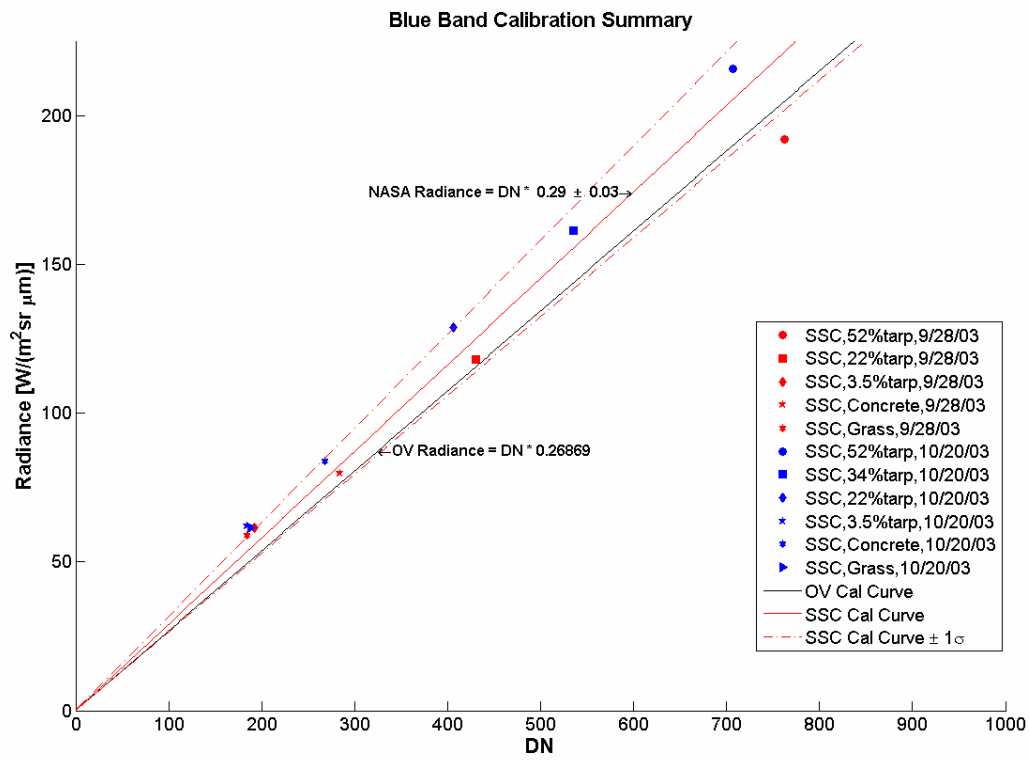


Figure A-1. Blue band composite summary result plot.

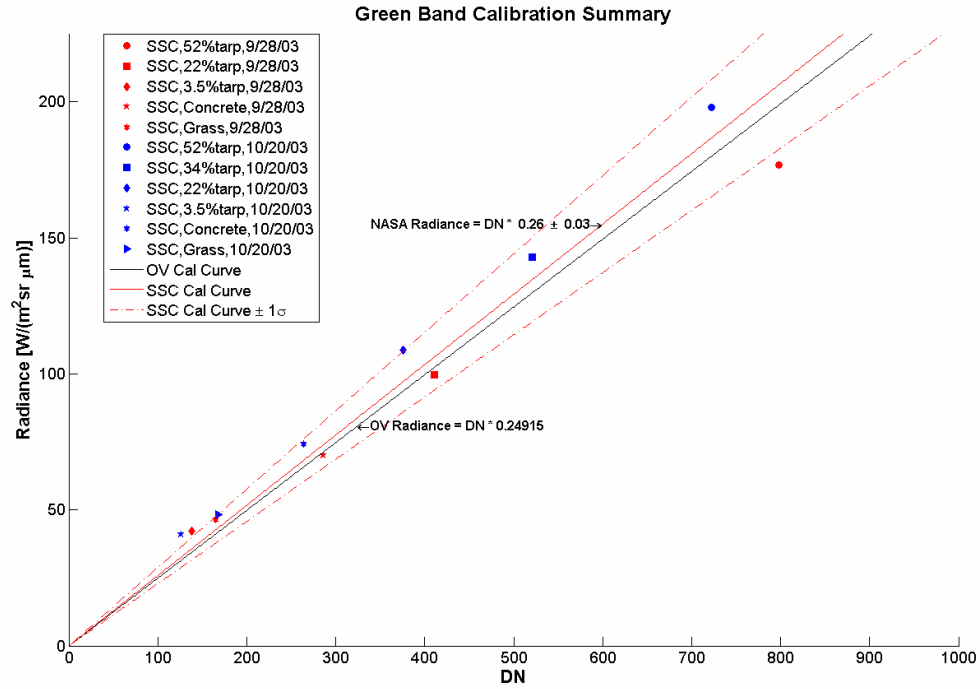


Figure A-2. Green band composite summary result plot.

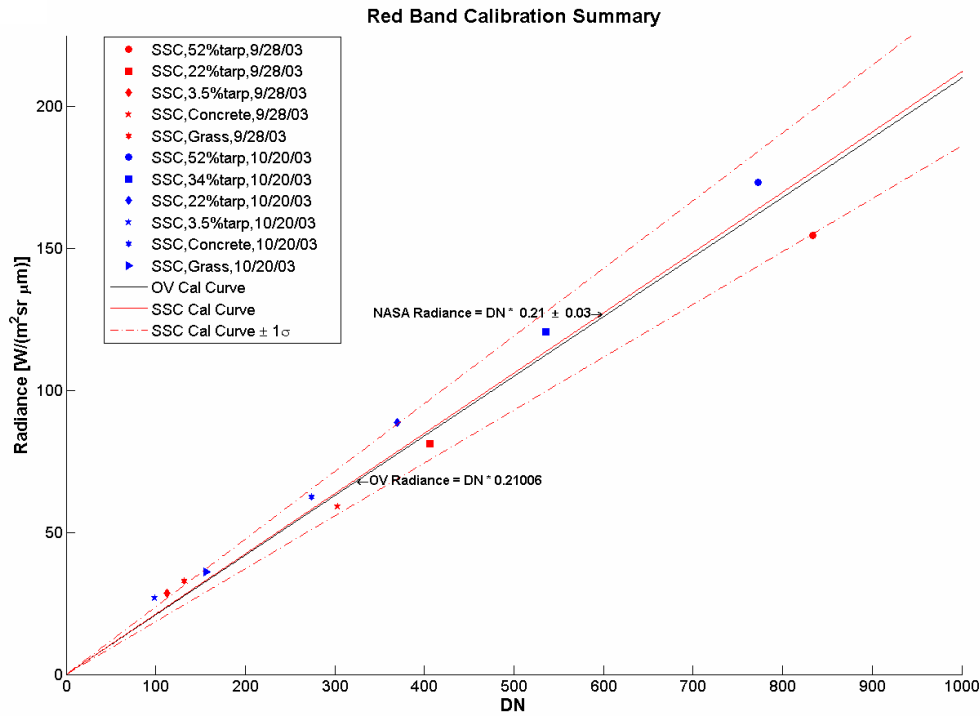


Figure A-3. Red band composite summary result plot.

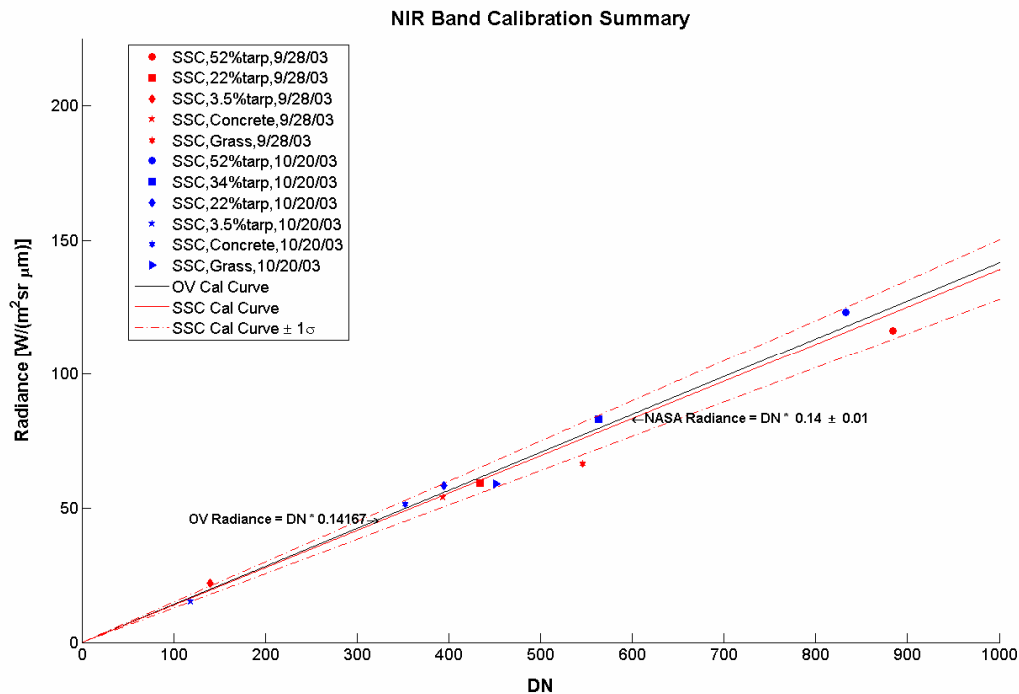


Figure A-4. NIR band composite summary result plot.

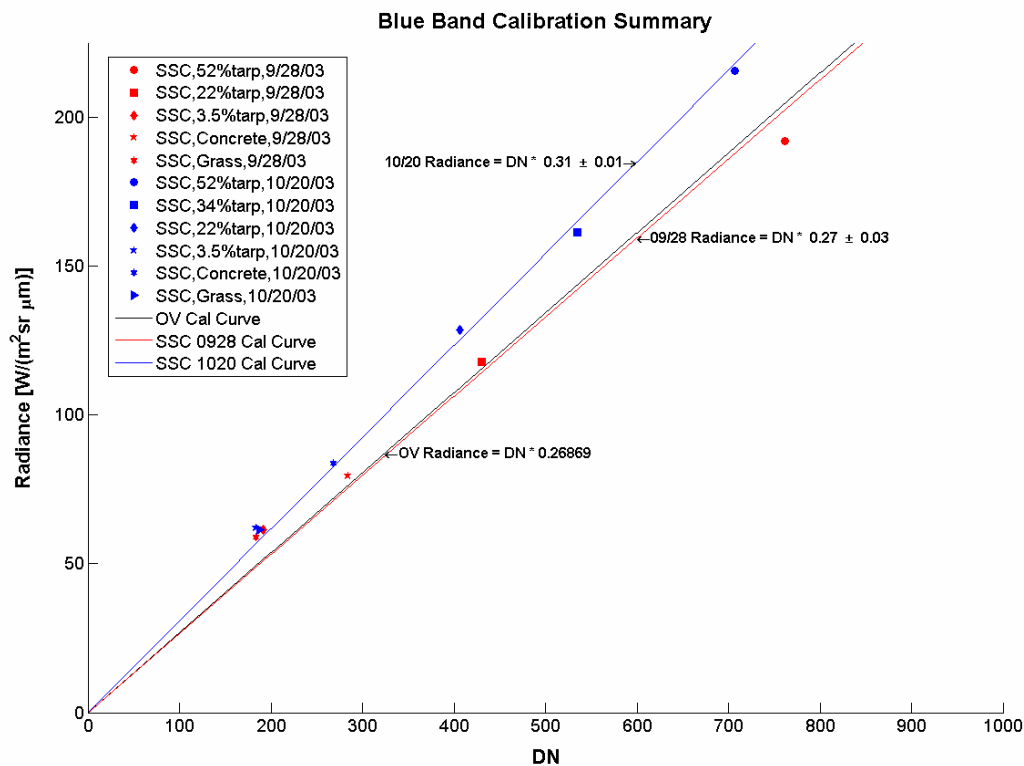


Figure A-5. Blue band individual day result plot.

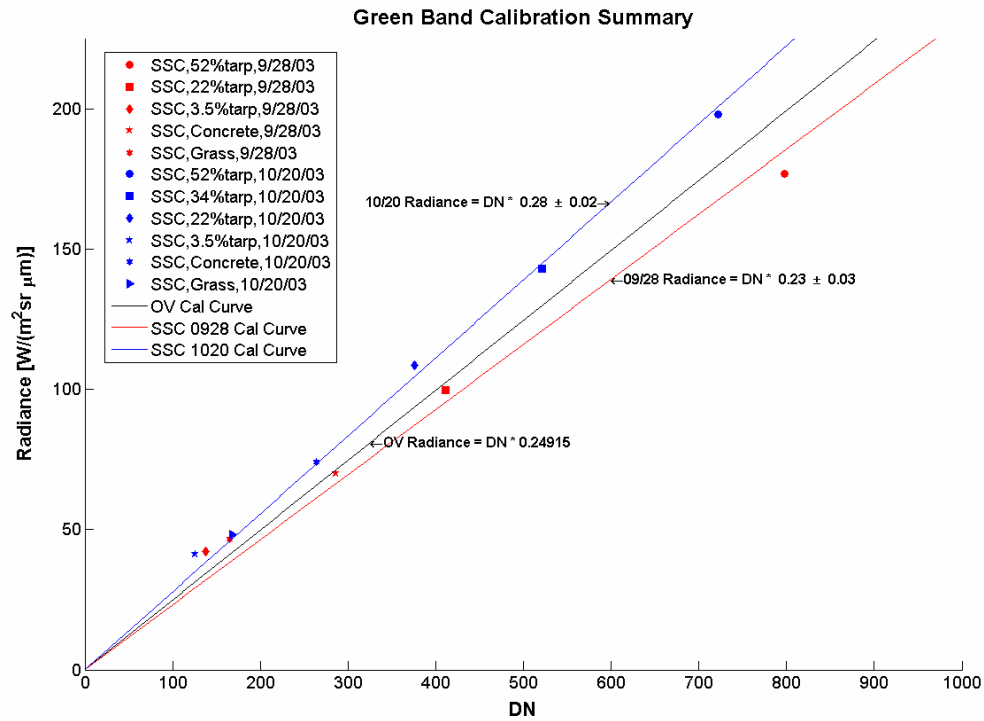


Figure A-6. Green band individual day result plot.

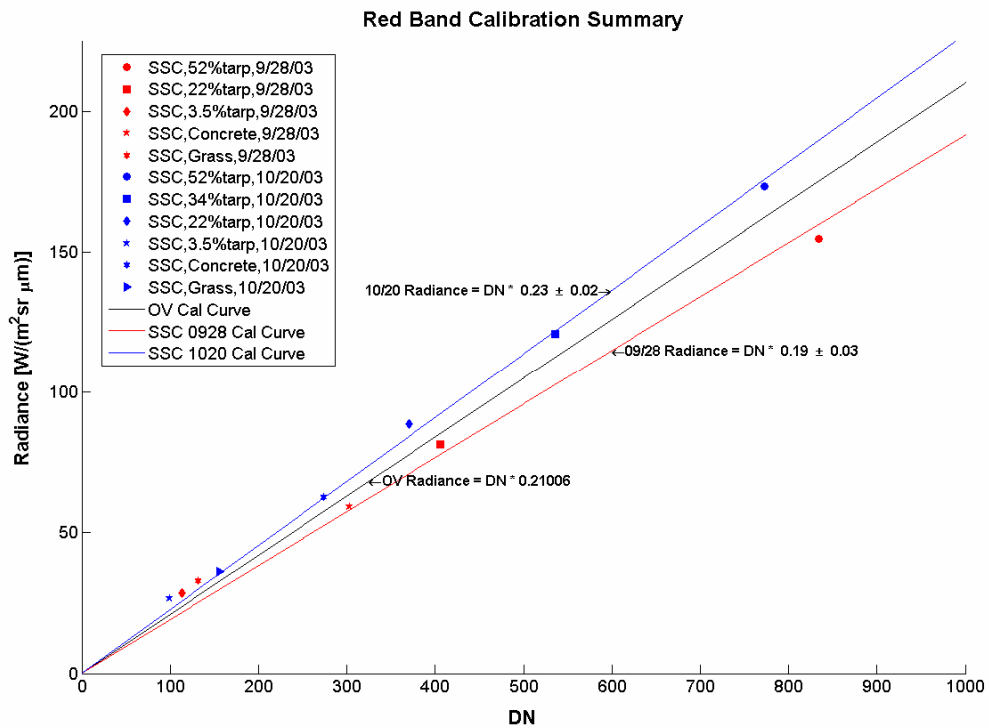


Figure A-7. Red band individual day result plot.

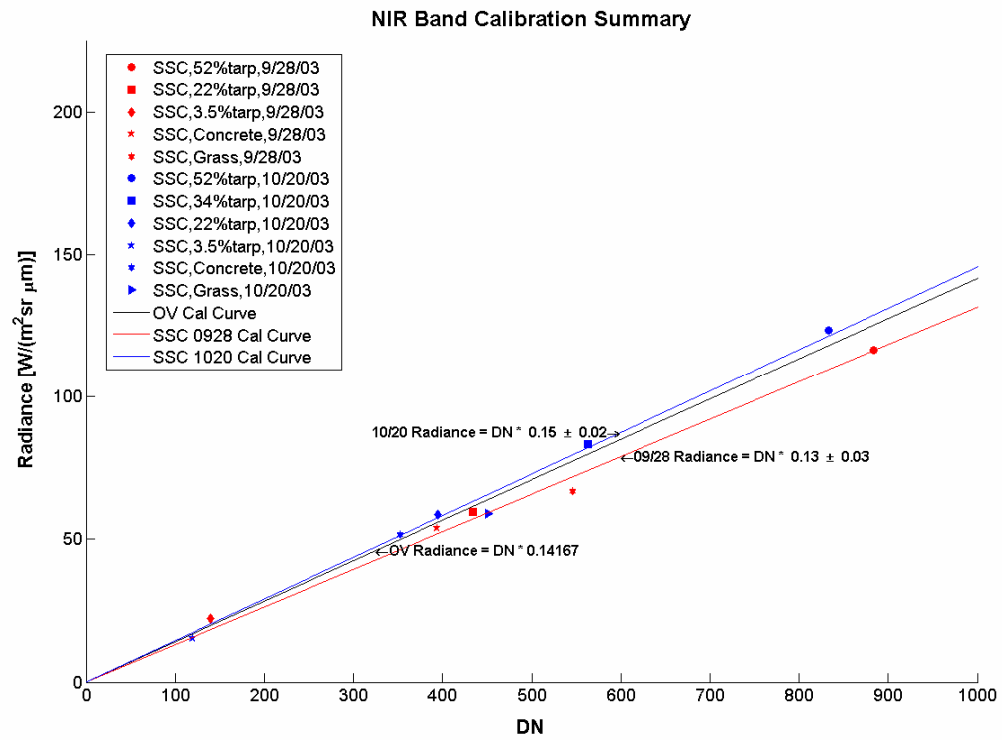


Figure A-8. NIR band individual day result plot.

Appendix B. Edge Response Functions Measured During the Spatial Resolution Characterization

B.1. Image ID: 14442; Acquisition Date: September 17, 2003



Figure B-1. OrbView-3 panchromatic image (*Georaw*) of the SSC edge targets and area selected for the edge response analysis in the cross-scan direction (yellow box).



Figure B-2. OrbView-3 panchromatic image (*Basic*) of the SSC edge targets and area selected for the edge response analysis in the cross-scan direction (yellow box).

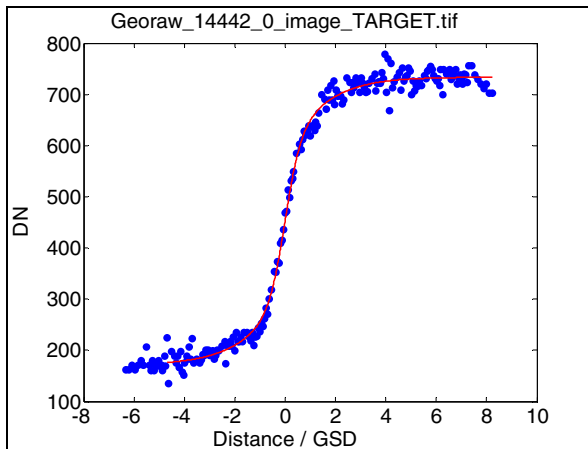


Figure B-3. Cross-scan direction edge response extracted from the *Georaw* image.

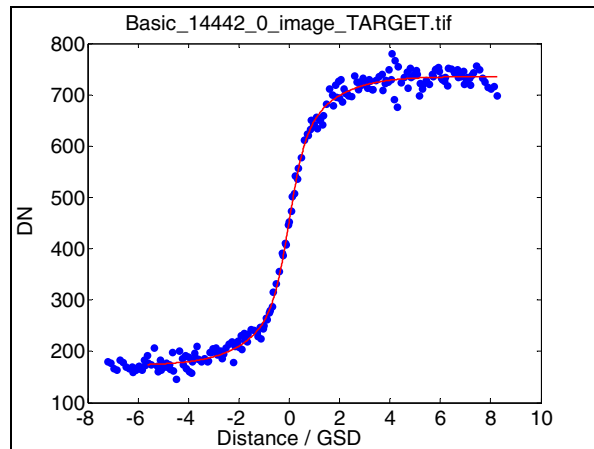


Figure B-4. Cross-scan direction edge response extracted from the *Basic* image.

B.2. Image ID: 14442; Acquisition Date: September 17, 2003

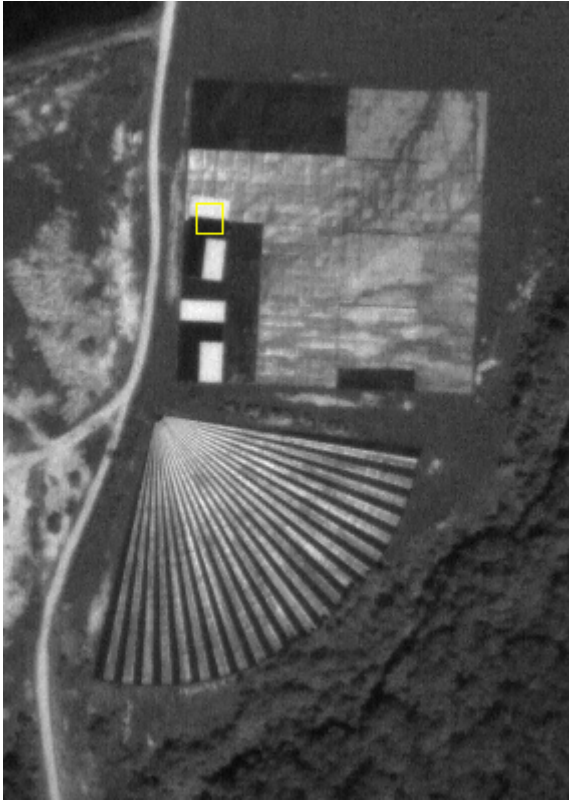


Figure B-5. OrbView-3 panchromatic image (*Georaw*) of the SSC edge targets and area selected for the edge response analysis in the along-scan direction (yellow box).



Figure B-6. OrbView-3 panchromatic image (*Basic*) of the SSC edge targets and area selected for the edge response analysis in the along-scan direction (yellow box).

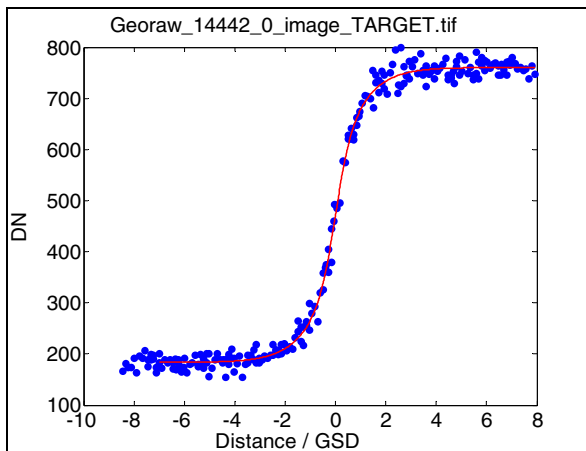


Figure B-7. Along-scan direction edge response extracted from the *Georaw* image.

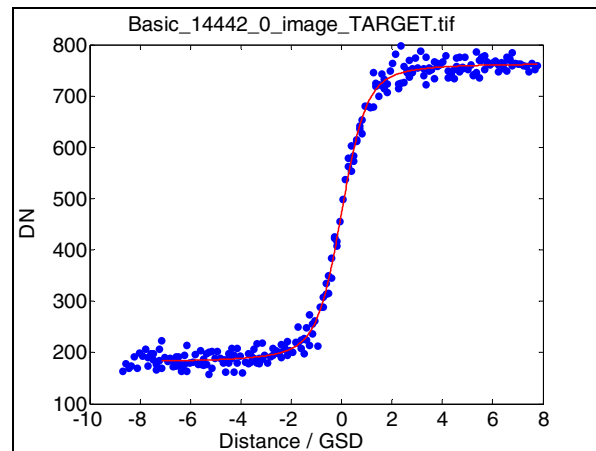


Figure B-8. Along-scan direction edge response extracted from the *Basic* image.

B.3. Image ID: 24790; Acquisition Date: December 12, 2003



Figure B-9. OrbView-3 panchromatic image (*Georaw*) of the SSC edge targets and area selected for the edge response analysis in the cross-scan direction (yellow box).



Figure B-10. OrbView-3 panchromatic image (*Basic*) of the SSC edge targets and area selected for the edge response analysis in the cross-scan direction (yellow box).

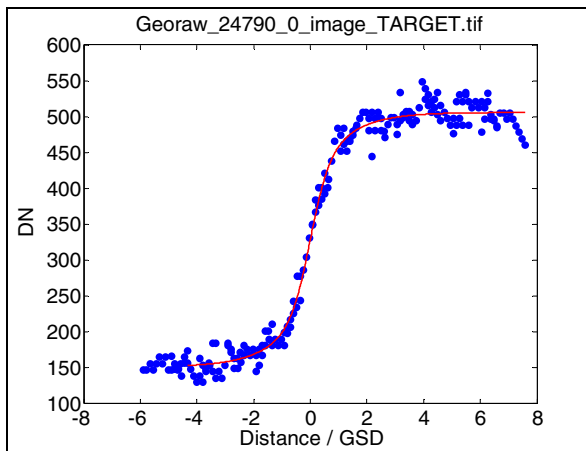


Figure B-11. Cross-scan direction edge response extracted from the *Georaw* image.

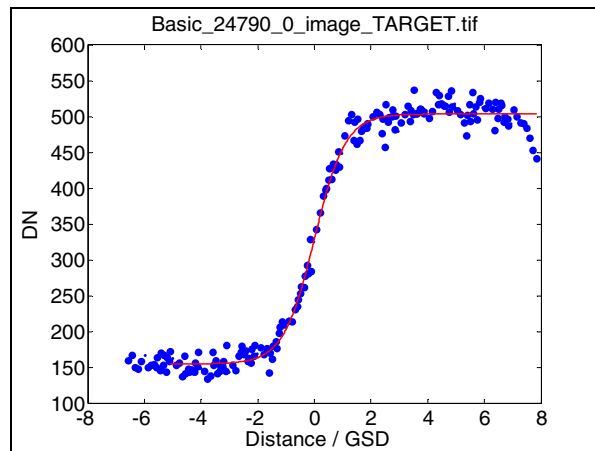


Figure B-12. Cross-scan direction edge response extracted from the *Basic* image.

B.4. Image ID: 24790; Acquisition Date: December 12, 2003



Figure B-13. OrbView-3 panchromatic image (*Georaw*) of the SSC edge targets and area selected for the edge response analysis in the along-scan direction (yellow box).

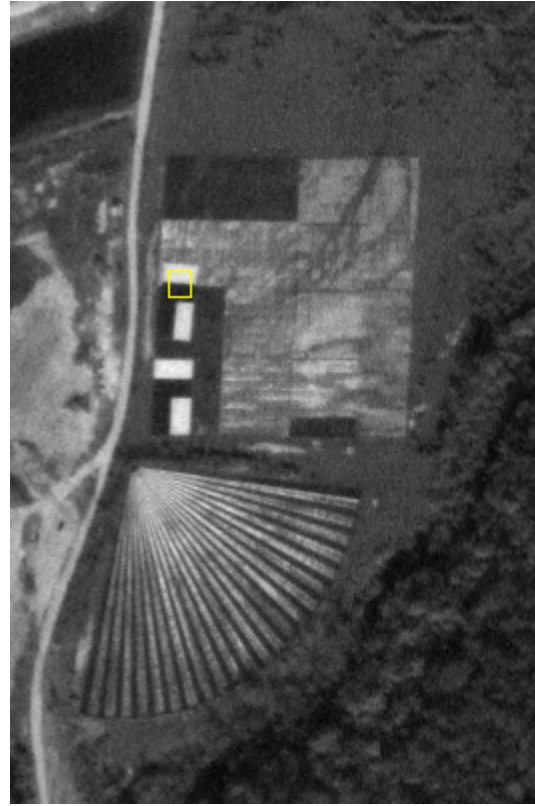


Figure B-14. OrbView-3 panchromatic image (*Basic*) of the SSC edge targets and area selected for the edge response analysis in the along-scan direction (yellow box).

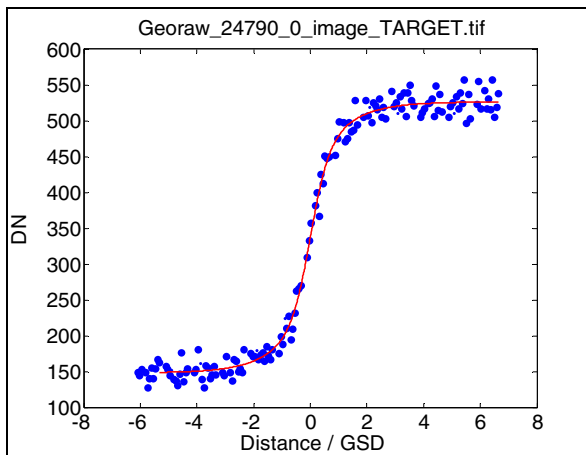


Figure B-15. Along-scan direction edge response extracted from the *Georaw* image.

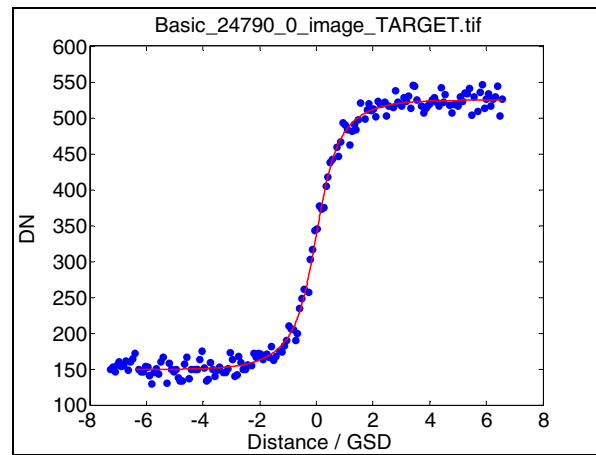


Figure B-16. Along-scan direction edge response extracted from the *Basic* image.

B.5. Image ID: 22760; Acquisition Date: December 15, 2003



Figure B-17. OrbView-3 panchromatic image (*Georaw*) of the SSC edge targets and area selected for the edge response analysis in the cross-scan direction (yellow box).



Figure B-18. OrbView-3 panchromatic image (*Basic*) of the SSC edge targets and area selected for the edge response analysis in the cross-scan direction (yellow box).

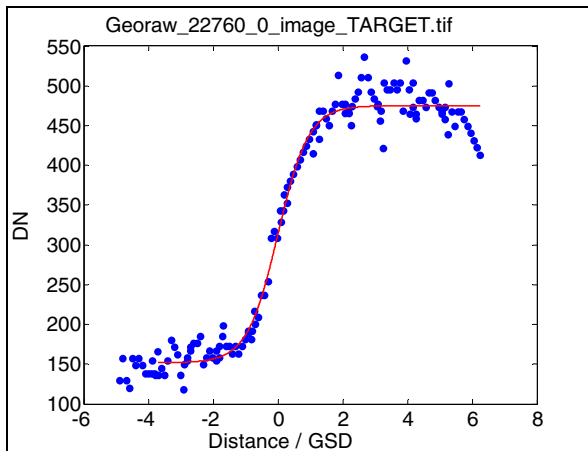


Figure B-19. Cross-scan direction edge response extracted from the *Georaw* image.

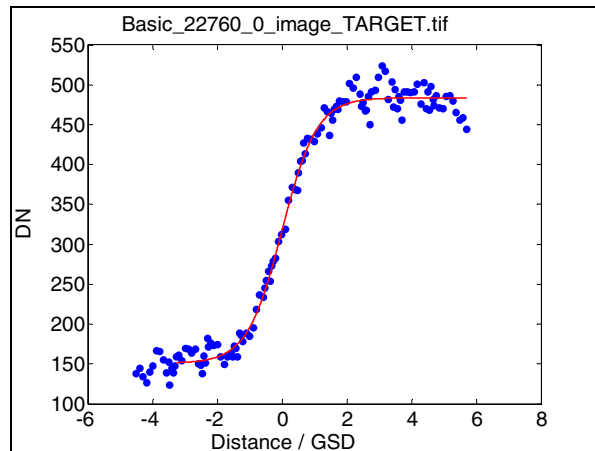


Figure B-20. Cross-scan direction edge response extracted from the *Basic* image.

B.6. Image ID: 22760; Acquisition Date: December 15, 2003

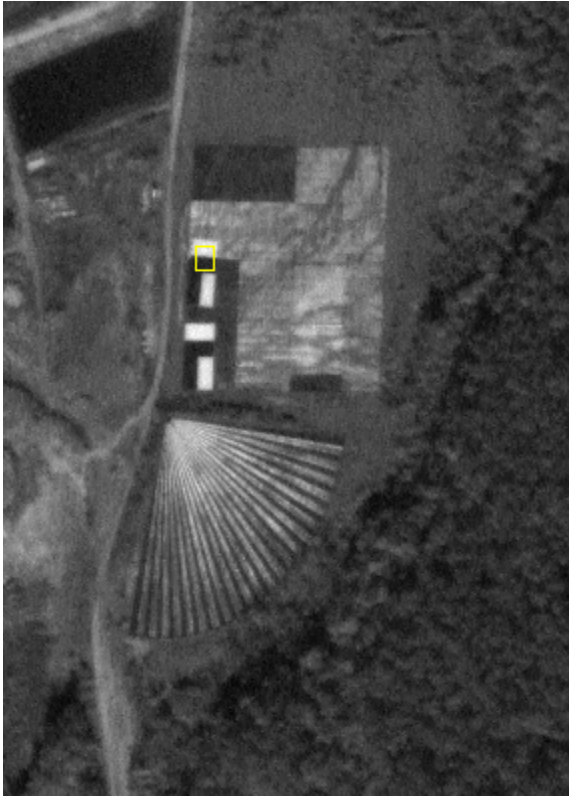


Figure B-21. OrbView-3 panchromatic image (*Georaw*) of the SSC edge targets and area selected for the edge response analysis in the along-scan direction (yellow box).



Figure B-22. OrbView-3 panchromatic image (*Basic*) of the SSC edge targets and area selected for the edge response analysis in the along-scan direction (yellow box).

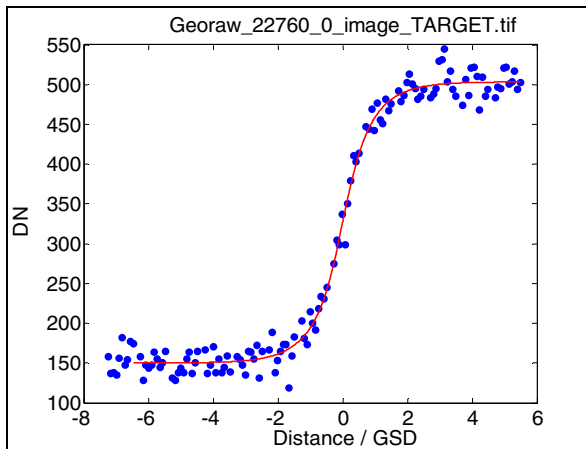


Figure B-23. Along-scan direction edge response extracted from the *Georaw* image.

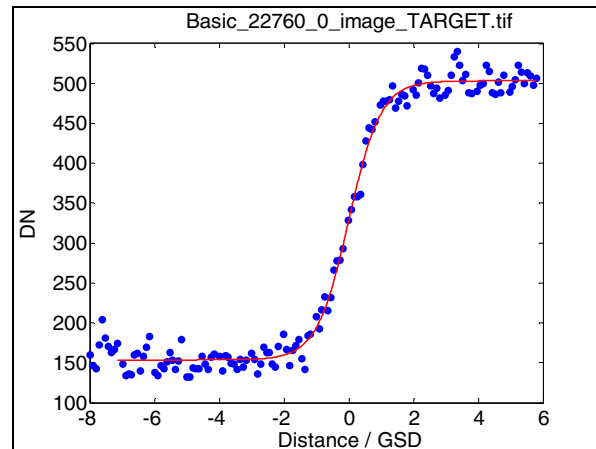


Figure B-24. Along-scan direction edge response extracted from the *Basic* image.

B.7. Image ID: 23539; Acquisition Date: December 26, 2003

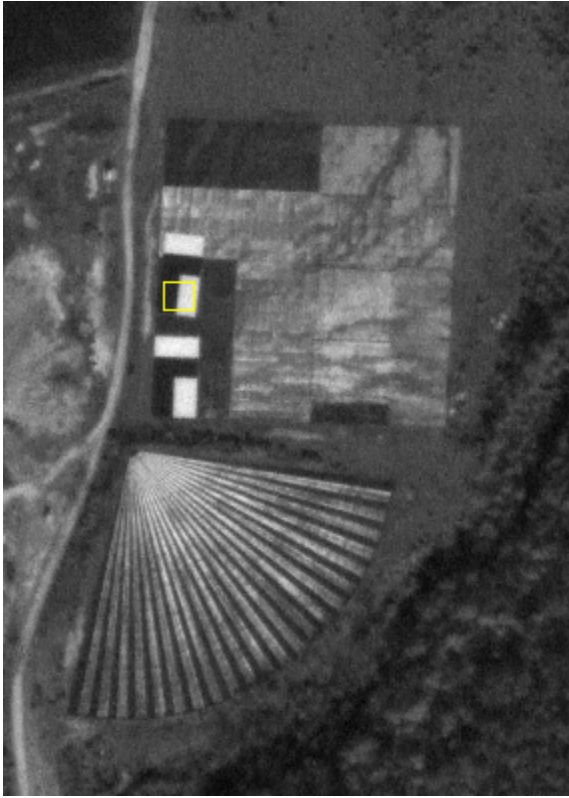


Figure B-25. OrbView-3 panchromatic image (*Georaw*) of the SSC edge targets and area selected for the edge response analysis in the cross-scan direction (yellow box).

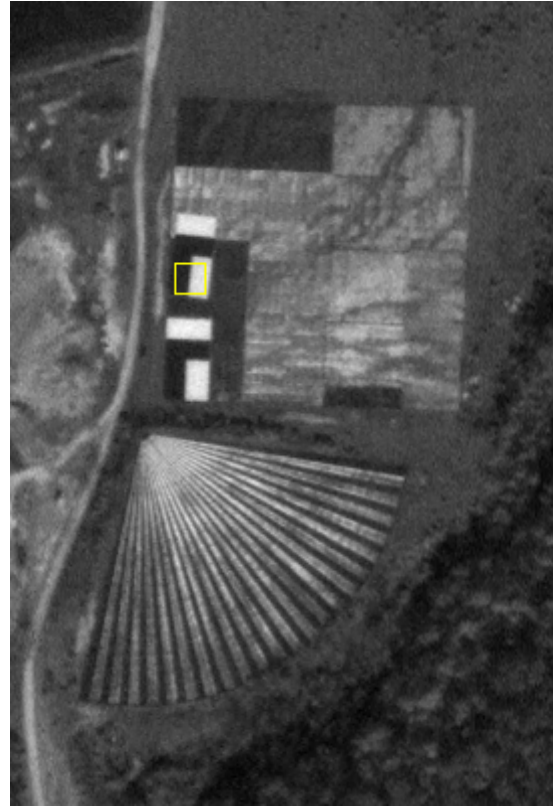


Figure B-26. OrbView-3 panchromatic image (*Basic*) of the SSC edge targets and area selected for the edge response analysis in the cross-scan direction (yellow box).

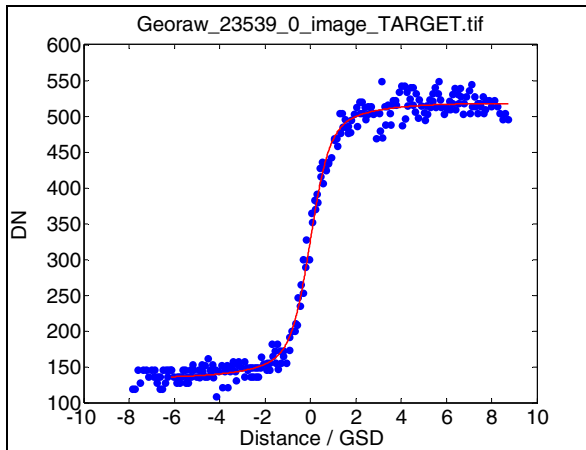


Figure B-27. Cross-scan direction edge response extracted from the *Georaw* image.

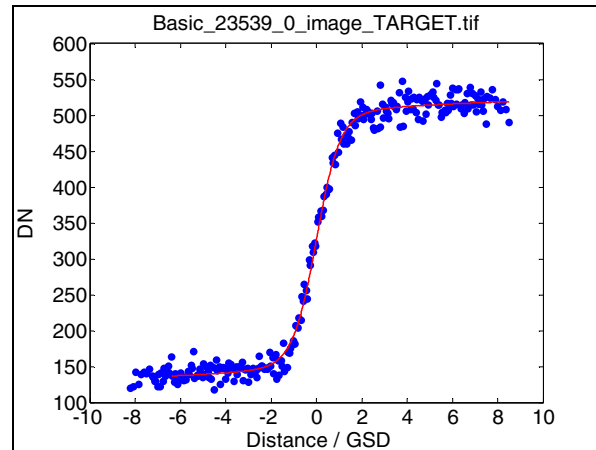


Figure B-28. Cross-scan direction edge response extracted from the *Basic* image.

B.8. Image ID: 23539; Acquisition Date: December 26, 2003

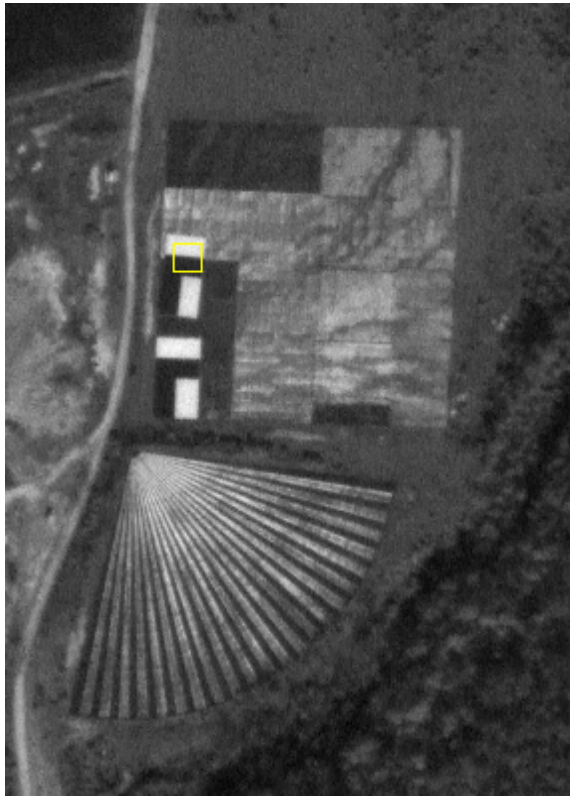


Figure B-29. OrbView-3 panchromatic image (*Georaw*) of the SSC edge targets and area selected for the edge response analysis in the along-scan direction (yellow box).

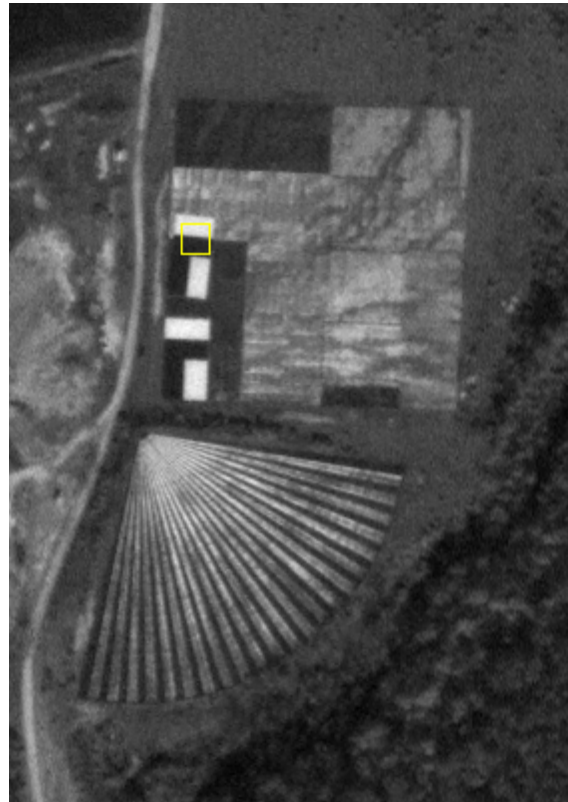


Figure B-30. OrbView-3 panchromatic image (*Basic*) of the SSC edge targets and area selected for the edge response analysis in the along-scan direction (yellow box).

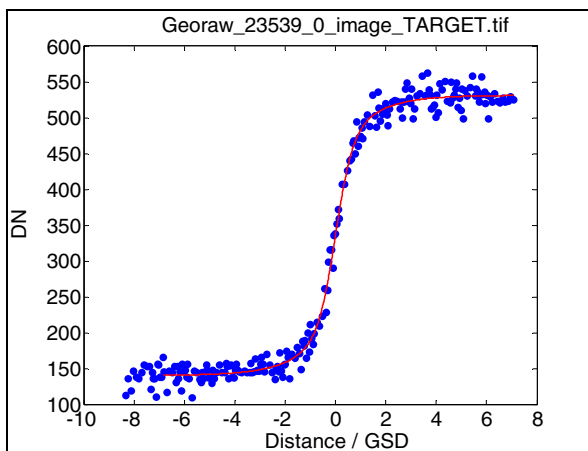


Figure B-31. Along-scan direction edge response extracted from the *Georaw* image.

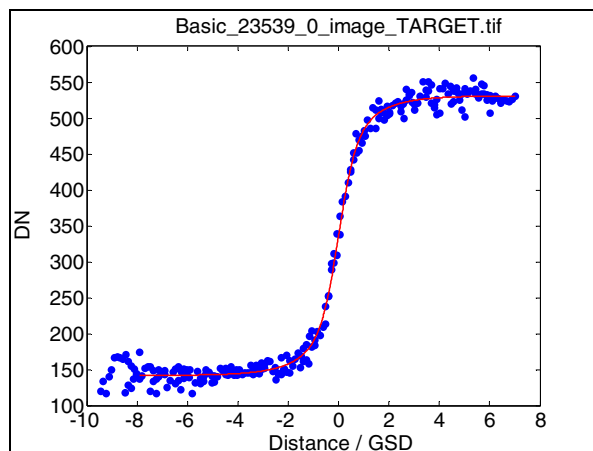


Figure B-32. Along-scan direction edge response extracted from the *Basic* image.

B.9. Image ID: 24515, Acquisition Date: January 12, 2004



Figure B-33. OrbView-3 panchromatic image (*Georaw*) of the SSC edge targets and area selected for the edge response analysis in the cross-scan direction (yellow box).



Figure B-34. OrbView-3 panchromatic image (*Basic*) of the SSC edge targets and area selected for the edge response analysis in the cross-scan direction (yellow box).

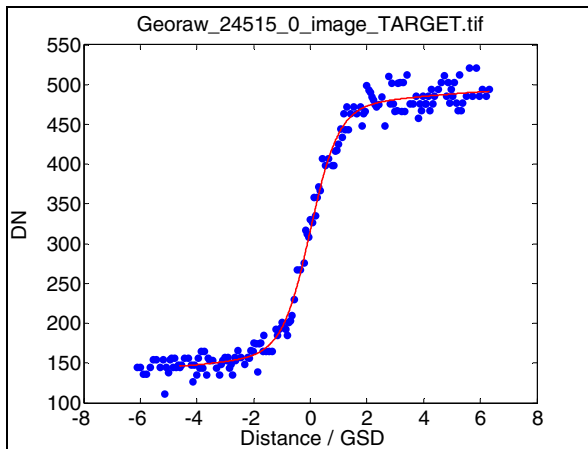


Figure B-35. Cross-scan direction edge response extracted from the *Georaw* image.

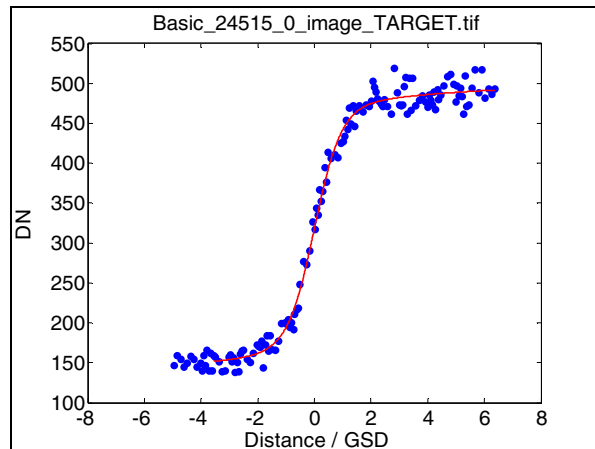


Figure B-36. Cross-scan direction edge response extracted from the *Basic* image.

B.10. Image ID: 24515, Acquisition Date: January 12, 2004



Figure B-37. OrbView-3 panchromatic image (*Georaw*) of the SSC edge targets and area selected for the edge response analysis in the along-scan direction (yellow box).



Figure B-38. OrbView-3 panchromatic image (*Basic*) of the SSC edge targets and area selected for the edge response analysis in the along-scan direction (yellow box).

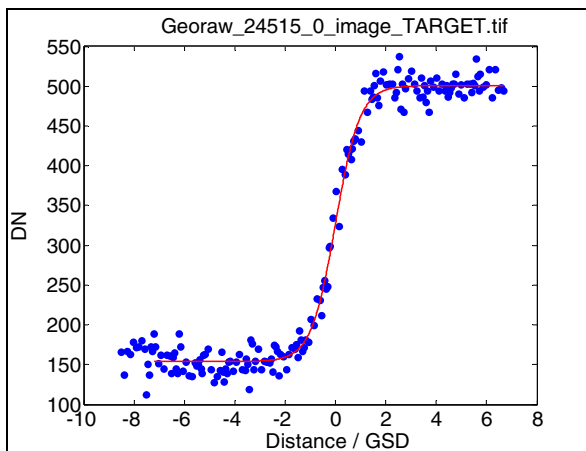


Figure B-39. Along-scan direction edge response extracted from the *Georaw* image.

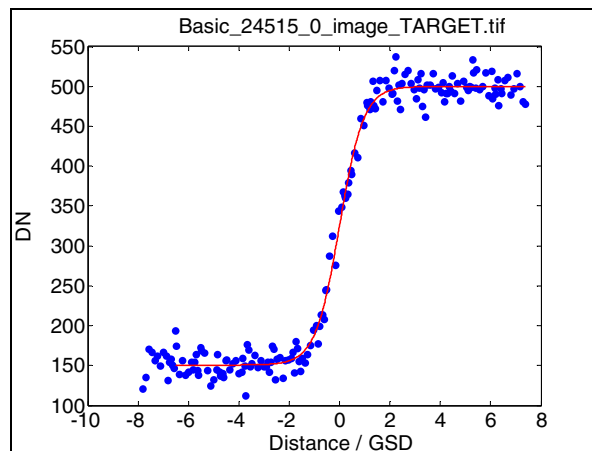


Figure B-40. Along-scan direction edge response extracted from the *Basic* image.

Appendix C. Geopositional Accuracy Details

C.1. Mathematical Definitions

Let the differences between image and reference coordinates be defined as follows:

$$\begin{aligned}\Delta X_i &= X_{image,i} - X_{reference,i} \\ \Delta Y_i &= Y_{image,i} - Y_{reference,i}\end{aligned}\tag{2}$$

Where ΔX is the Easting difference, or delta, and ΔY is the Northing difference. The magnitude of individual horizontal errors may then be defined as follows:

$$\Delta R_i = \sqrt{\Delta X_i^2 + \Delta Y_i^2}\tag{3}$$

This horizontal magnitude can be used to compute the empirical versions of Circular Error. Circular Error at the 90% level (CE_{90}) is just the 90th percentile of ΔR , and Circular Error at the 95th percentile level (CE_{95}) is the 95th percentile of ΔR .

This empirical approach is simple to implement, but it can be susceptible to small datasets or the presence of outliers, so it is desirable to use alternative error measures. Root Mean Square Error (RMSE) is a statistic that is often used. RMSE is defined in both directions in the following manner:

$$\begin{aligned}RMSE_x &= \sqrt{\sum \frac{\Delta X_i^2}{n}} \\ RMSE_y &= \sqrt{\sum \frac{\Delta Y_i^2}{n}}\end{aligned}\tag{4}$$

Where n is the total number of reference points that could be found in a given image. Total horizontal error is then sometimes characterized as the vector sum of the X and Y error:

$$RMSE_{net} = \sqrt{RMSE_x^2 + RMSE_y^2}\tag{5}$$

However, RMSE does not separate the effects of systematic and random error. Systematic and random error may be estimated if it is assumed that the systematic error is a displacement or “bias” that is unknown *a priori*. The bias, designated here as μ_H , is the vector sum of the average error in the X and the Y :

$$\mu_H = \sqrt{(\overline{\Delta X})^2 + (\overline{\Delta Y})^2}\tag{6}$$

The magnitude of horizontal random error, σ_c , is shown by Greenwalt and Shultz (1962) to be closely approximated by the average of the standard deviations of the X and Y differences ($\sigma_{\Delta X}$ and $\sigma_{\Delta Y}$ in this treatment) in cases where the error distribution is approximately circular:

$$\sigma_c \cong \frac{\sigma_{\Delta X} + \sigma_{\Delta Y}}{2}\tag{7}$$

It is important to note that the standard deviation computations differ from the RMSE computation in that they subtract the mean and consequently use $n-1$ weighting instead of n weighting.

Having computed estimates of random error and bias, two important ratios may be computed. The first is the ratio of minimum to maximum random error between the X and Y directions:

$$\frac{\min(\sigma_{\Delta X}, \sigma_{\Delta Y})}{\max(\sigma_{\Delta X}, \sigma_{\Delta Y})} \quad (8)$$

Greenwalt and Schultz (1962) showed that as long as this ratio is greater than 0.6, error distributions may be adequately described with Circular Error statistics.

The second important ratio is that of bias to random error:

$$\frac{\mu_H}{\sigma_C} \quad (9)$$

This ratio allows easy discrimination of images that are more or less affected by bias. Ager (2004) uses a threshold of 0.1 to identify datasets that are unbiased. For datasets with μ_H/σ_C below that threshold, Circular Error may be calculated from RMSE values as given in the National Standard for Spatial Data Accuracy (NSSDA) (FGDC, 1998). Above that threshold, Circular Error should be computed with an alternate method, such as the empirical approach described above in Eq. (3) and its following paragraph.

In this effort, both empirical and RMSE-based estimates for Circular Error have been reported. The following conditions should guide which estimate should be preferred:

$$\begin{aligned} \frac{\mu_H}{\sigma_C} < 0.1 : & \text{compute Circular Error from RMSE – based methods} \\ \frac{\mu_H}{\sigma_C} \geq 0.1 : & \text{compute Circular Error from empirical method} \end{aligned} \quad (10)$$

Note that CE_{95} based on RMSE is defined as $Accuracy_r$ in the NSSDA and that CE_{90} based on RMSE was preferred in the previous United States National Map Accuracy Standards (U.S. Bureau of the Budget, 1947) and was known as Circular Map Accuracy Standard (CMAS). Drawing from the NSSDA, $Accuracy_r$ is given approximately as follows:

$$Accuracy_r \sim 2.4477 * 0.5 * (RMSE_x + RMSE_y) \quad (11)$$

And CMAS may be computed similarly:

$$CMAS \sim 2.1460 * 0.5 * (RMSE_x + RMSE_y) \quad (12)$$

C.2. Results by Acquisition

Table C-1. Geopositional point-by-point computations, September 17, 2003.

Point	diff. in X (ΔX)	(ΔX^2)	diff. in Y (ΔY)	(ΔY^2)	magnitude horiz. diff. (ΔR)
1-A	-5.82	33.88	-5.05	25.50	7.71
1-B	-6.67	44.54	-4.31	18.61	7.95
1-C	-6.68	44.62	-4.82	23.26	8.24
1-D	-6.32	39.88	-4.51	20.30	7.76
1-E	-5.94	35.24	-4.85	23.48	7.66
1-F	-6.55	42.88	-4.41	19.47	7.90
1-G	-5.93	35.16	-5.12	26.18	7.83
1-H	-6.51	42.41	-4.40	19.40	7.86
1-I	-6.35	40.28	-5.23	27.38	8.23
2-A	-6.57	43.11	-4.95	24.51	8.22
2-B	-6.35	40.27	-4.85	23.51	7.99
2-C	-6.94	48.12	-4.44	19.70	8.24
2-D	-6.08	36.94	-5.06	25.57	7.91
2-E	-6.40	40.99	-4.99	24.91	8.12
2-F	-6.31	39.84	-5.71	32.64	8.51
2-G	-6.16	37.93	-4.50	20.21	7.62
2-I	-6.67	44.44	-5.03	25.33	8.35
3-A	-6.21	38.54	-5.60	31.38	8.36
3-B	-5.36	28.71	-5.89	34.66	7.96
3-C	-5.24	27.50	-5.27	27.75	7.43
3-D	-5.07	25.70	-5.95	35.40	7.82
3-E	-6.30	39.68	-5.28	27.92	8.22
3-F	-5.65	31.91	-5.80	33.63	8.10
3-G	-6.65	44.25	-5.72	32.68	8.77
3-H	-5.70	32.49	-5.85	34.25	8.17
3-I	-5.99	35.88	-5.57	31.07	8.18
4-A	-4.92	24.18	-5.28	27.89	7.22
4-B	-4.61	21.26	-5.90	34.85	7.49
4-C	-5.40	29.17	-5.55	30.79	7.74
4-D	-4.40	19.36	-5.58	31.18	7.11
4-E	-5.45	29.74	-6.23	38.84	8.28
4-F	-4.73	22.38	-6.06	36.72	7.69
4-G	-4.62	21.30	-6.39	40.82	7.88
4-H	-4.81	23.17	-6.33	40.02	7.95
4-I	-4.93	24.33	-6.45	41.56	8.12
5	-5.67	32.16	-5.06	25.58	7.60
6	-6.22	38.69	-4.81	23.16	7.86
7	-6.13	37.60	-5.41	29.29	8.18
8	-6.46	41.71	-5.15	26.51	8.26
9	-6.36	40.42	-5.13	26.27	8.17
Note: All measurements are in meters.					

Table C-2. Geopositional accuracy results for acquisition on September 17, 2003.

Remote Sensing System		OrbView-3	
Acquisition Date	9/17/2003	Imagery Band	PAN
Number Targets Used			
<i>n</i>	40		
NSSDA requires 20 or more points.			
ΔX & ΔY			
Average ΔX	-5.88 m	Average ΔY	-5.31 m
Standard Deviation ΔX	0.69 m	Standard Deviation ΔY	0.59 m
RMSE X	5.92 m	RMSE Y	5.34 m
Test for Departure from Circular Distribution		Root Mean Square Error Summary	
St. Dev. Min Max Ratio	0.84	RMSE _{net}	7.97 m
St. Dev. Min Max Ratio should be at least 0.6 for Circular Error assumptions.			
Bias & Random Error Estimates			
μ_H (Bias)	7.92 m	σ_C (Circular Standard Error)	0.64 m
μ_H/σ_C	12.40		
If μ_H/σ_C is greater than 0.1, then error calculations should account for bias.			
Circular Error			
CMAS (<i>CE</i> ₉₀)	12.08 m	Empirical <i>CE</i> ₉₀	8.32 m
NSSDA Accuracy _r (<i>CE</i> ₉₅)	13.78 m	Empirical <i>CE</i> ₉₅	8.44 m
NSSDA & CMAS assume bivariate normal distributions with zero bias.			
Note: The μ_H/σ_C value in this case (12.40) strongly indicates against characterizing this data with a zero bias assumption. CMAS and NSSDA Accuracy _r are included here for reference only. When these RMSE-based calculations have been applied to similar data at SSC, overestimation of 10-50% has been demonstrated.			

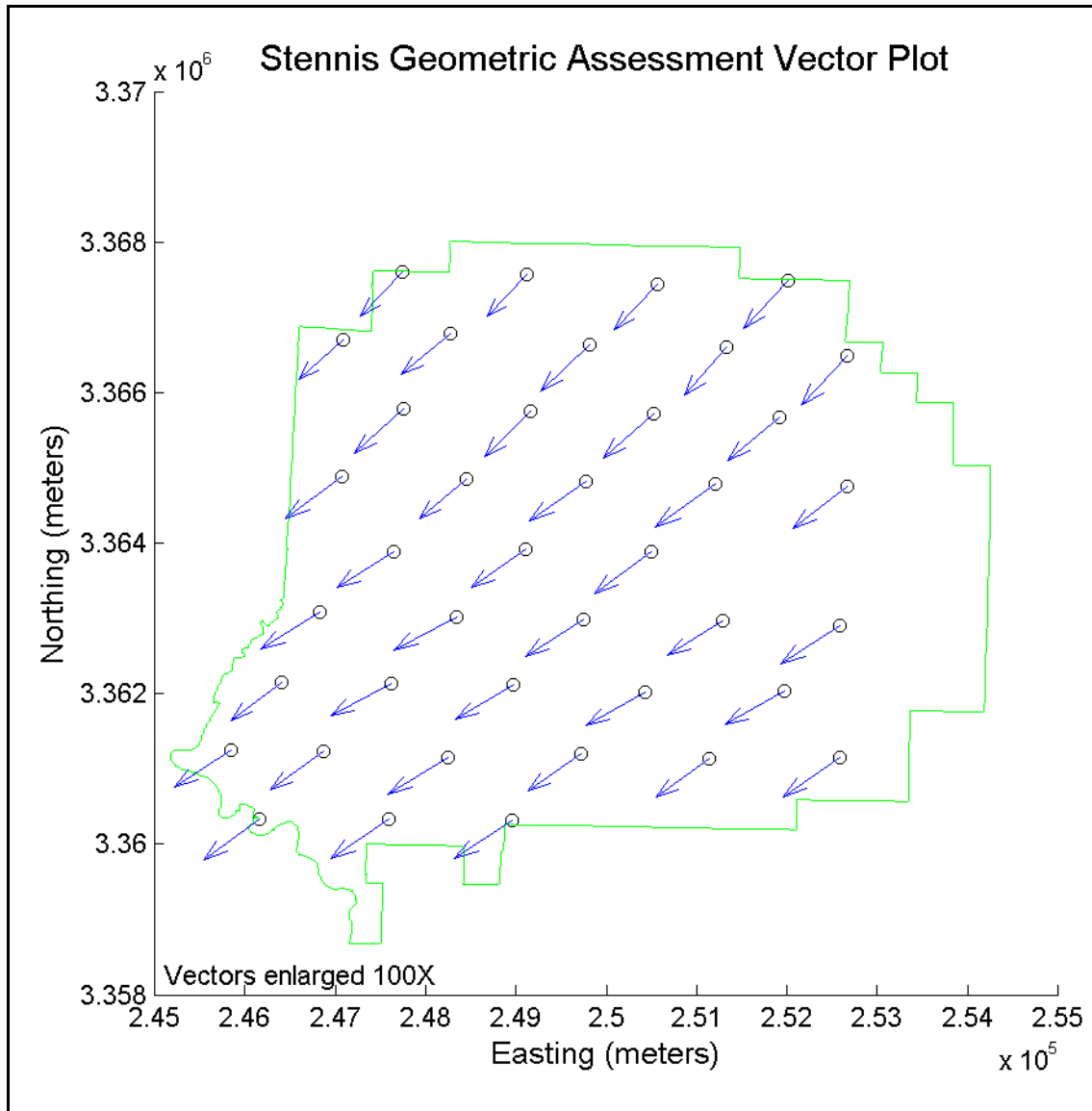


Figure C-1. Vector plot of target errors for acquisition on September 17, 2003.

Table C-3. Geopositional point-by-point computations, December 12, 2003.

Point	diff. in X (ΔX)	(ΔX^2)	diff. in Y (ΔY)	(ΔY^2)	magnitude horiz. diff. (ΔR)
1-A	-3.24	10.52	1.33	1.76	3.50
1-C	-4.50	20.28	1.06	1.13	4.63
1-D	-4.08	16.65	1.42	2.02	4.32
1-E	-3.87	14.95	1.29	1.67	4.08
1-F	-4.34	18.87	1.58	2.50	4.62
1-H	-4.27	18.23	1.61	2.58	4.56
1-I	-4.16	17.31	0.76	0.58	4.23
1-J	-4.80	23.00	1.48	2.20	5.02
2-B	-4.23	17.88	2.08	4.33	4.71
2-C	-4.78	22.87	1.54	2.36	5.02
2-D	-3.88	15.09	1.87	3.48	4.31
2-E	-4.72	22.24	1.38	1.92	4.91
2-I	-4.54	20.63	1.14	1.30	4.68
2-J	-4.50	20.21	1.04	1.08	4.61
3-A	-4.49	20.12	1.71	2.93	4.80
3-C	-4.06	16.51	1.78	3.16	4.44
3-D	-4.52	20.42	1.99	3.96	4.94
3-E	-5.20	27.00	1.65	2.71	5.45
3-F	-5.95	35.39	0.78	0.60	6.00
3-G	-5.52	30.42	1.27	1.62	5.66
3-H	-4.55	20.73	2.11	4.44	5.02
4-B	-4.44	19.68	1.05	1.11	4.56
4-C	-5.16	26.57	2.33	5.41	5.66
4-E	-4.61	21.29	1.59	2.53	4.88
4-H	-4.57	20.86	0.57	0.33	4.60
4-I	-4.84	23.38	1.49	2.21	5.06
5	-4.49	20.12	0.95	0.91	4.59
6	-3.58	12.84	1.71	2.91	3.97
7	-3.51	12.31	1.44	2.09	3.79
Note: All measurements are in meters.					

Table C-4. Geopositional accuracy results for acquisition on December 12, 2003.

Remote Sensing System		OrbView-3	
Acquisition Date	12/12/2003	Imagery Band	PAN
Number Targets Used			
<i>n</i>	29		
NSSDA requires 20 or more points.			
ΔX & ΔY			
Average ΔX	-4.46 m	Average ΔY	1.45 m
Standard Deviation ΔX	0.57 m	Standard Deviation ΔY	0.42 m
RMSE X	4.50 m	RMSE Y	1.51 m
Test for Departure from Circular Distribution		Root Mean Square Error Summary	
St. Dev. Min Max Ratio	0.74	RMSE _{net}	4.74 m
St. Dev. Min Max Ratio should be at least 0.6 for Circular Error assumptions.			
Bias & Random Error Estimates			
μ_H (Bias)	4.69 m	σ_C (Circular Standard Error)	0.50 m
μ_H/σ_C	9.43		
If μ_H/σ_C is greater than 0.1, then error calculations should account for bias.			
Circular Error			
CMAS (<i>CE</i> ₉₀)	6.44 m	Empirical <i>CE</i> ₉₀	5.57 m
NSSDA Accuracy _r (<i>CE</i> ₉₅)	7.35 m	Empirical <i>CE</i> ₉₅	5.68 m
NSSDA & CMAS assume bivariate normal distributions with zero bias.			
Note: The μ_H/σ_C value in this case (9.43) strongly indicates against characterizing this data with a zero bias assumption. CMAS and NSSDA Accuracy_r are included here for reference only. When these RMSE-based calculations have been applied to similar data at SSC, overestimation of 10-50% has been demonstrated.			

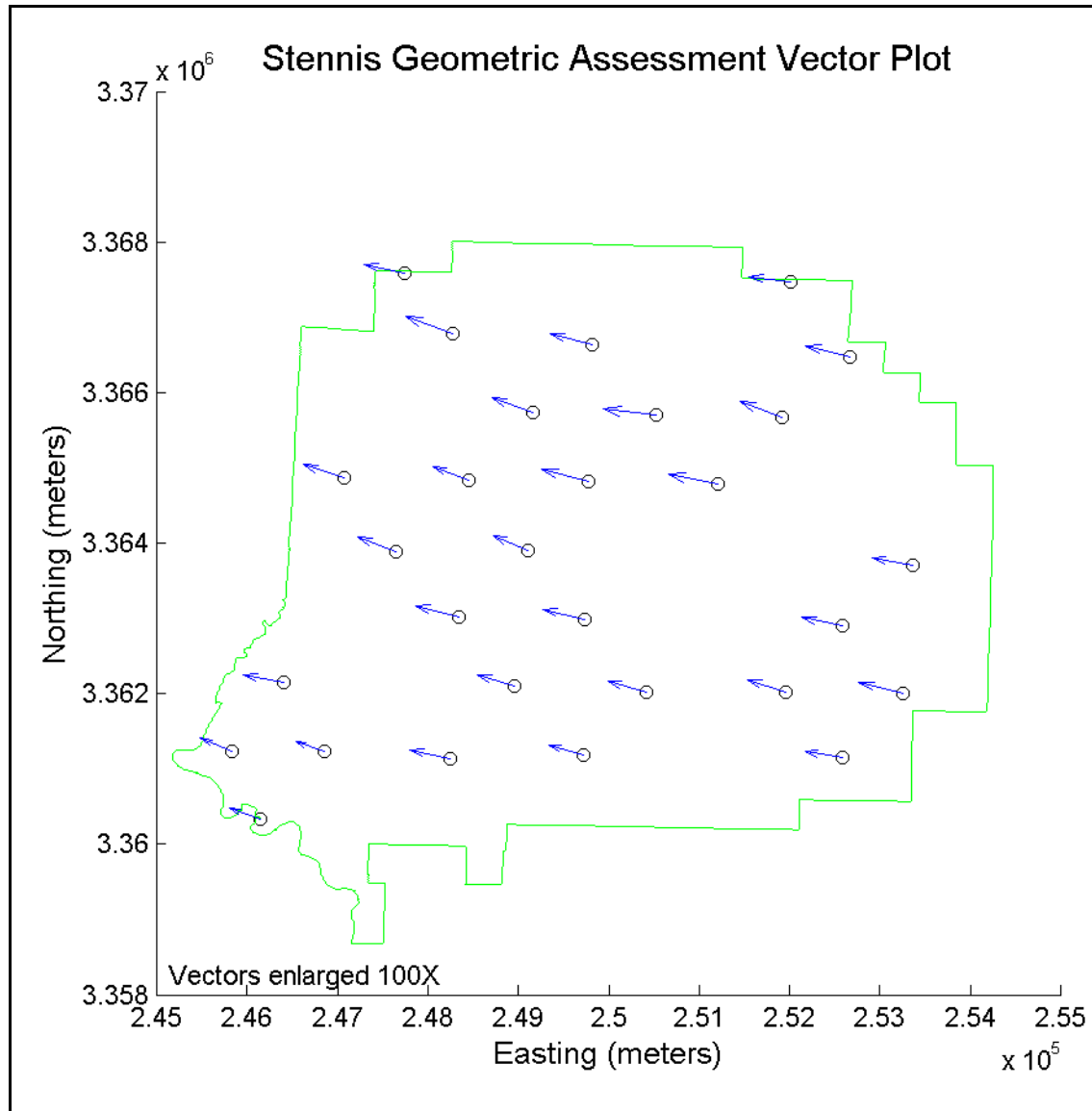


Figure C-2. Vector plot of target errors for acquisition on December 12, 2003.

Table C-5. Geopositional point-by-point computations, December 15, 2003.

Point	diff. in X (ΔX)	(ΔX^2)	diff. in Y (ΔY)	(ΔY^2)	magnitude horiz. diff. (ΔR)
1-C	-0.51	0.26	-8.96	80.26	8.97
1-D	-1.14	1.29	-8.54	72.90	8.61
1-E	0.10	0.01	-8.62	74.24	8.62
1-F	-1.24	1.53	-8.39	70.32	8.48
1-H	-0.31	0.09	-9.45	89.34	9.46
1-I	0.24	0.06	-8.93	79.74	8.93
1-J	-0.75	0.57	-9.39	88.15	9.42
2-B	-0.21	0.04	-9.85	97.10	9.86
2-C	-0.69	0.47	-9.48	89.79	9.50
2-D	-0.98	0.95	-10.04	100.84	10.09
2-E	-1.42	2.02	-9.01	81.20	9.12
2-I	-1.54	2.37	-9.11	82.99	9.24
2-J	-1.03	1.07	-9.74	94.81	9.79
3-A	-1.09	1.19	-10.62	112.74	10.67
3-D	-1.51	2.28	-11.00	120.96	11.10
3-E	-2.17	4.69	-10.33	106.65	10.55
3-G	-2.61	6.82	-10.68	113.96	10.99
3-H	-2.48	6.13	-10.84	117.42	11.12
3-K	-3.21	10.29	-10.39	107.99	10.88
4-B	-2.50	6.23	-10.94	119.57	11.22
4-C	-2.23	4.96	-10.68	114.08	10.91
4-E	-2.48	6.16	-10.53	110.90	10.82
4-H	-1.72	2.96	-11.31	127.96	11.44
4-I	-1.77	3.15	-10.55	111.30	10.70
5	-0.98	0.97	-8.61	74.10	8.66
6	0.43	0.18	-8.22	67.62	8.23
7	1.07	1.15	-8.48	71.86	8.54
Note: All measurements are in meters.					

Table C-6. Geopositional accuracy results for acquisition on December 15, 2003.

Remote Sensing System		OrbView-3	
Acquisition Date	12/15/2003	Imagery Band	PAN
Number Targets Used			
<i>n</i>	27		
NSSDA requires 20 or more points.			
ΔX & ΔY			
Average ΔX	-1.21 m	Average ΔY	-9.73 m
Standard Deviation ΔX	1.04 m	Standard Deviation ΔY	0.95 m
RMSE X	1.59 m	RMSE Y	9.77 m
Test for Departure from Circular Distribution		Root Mean Square Error Summary	
St. Dev. Min Max Ratio	0.91	RMSE _{net}	9.90 m
St. Dev. Min Max Ratio should be at least 0.6 for Circular Error assumptions.			
Bias & Random Error Estimates			
μ_H (Bias)	9.80 m	σ_C (Circular Standard Error)	1.00 m
μ_H/σ_C	9.83		
If μ_H/σ_C is greater than 0.1, then error calculations should account for bias.			
Circular Error			
CMAS (<i>CE</i> ₉₀)	12.19 m	Empirical <i>CE</i> ₉₀	11.11 m
NSSDA Accuracy _r (<i>CE</i> ₉₅)	13.90 m	Empirical <i>CE</i> ₉₅	11.25 m
NSSDA & CMAS assume bivariate normal distributions with zero bias.			
Note: The μ_H/σ_C value in this case (9.83) strongly indicates against characterizing this data with a zero bias assumption. CMAS and NSSDA Accuracy_r are included here for reference only. When these RMSE-based calculations have been applied to similar data at SSC, overestimation of 10-50% has been demonstrated.			

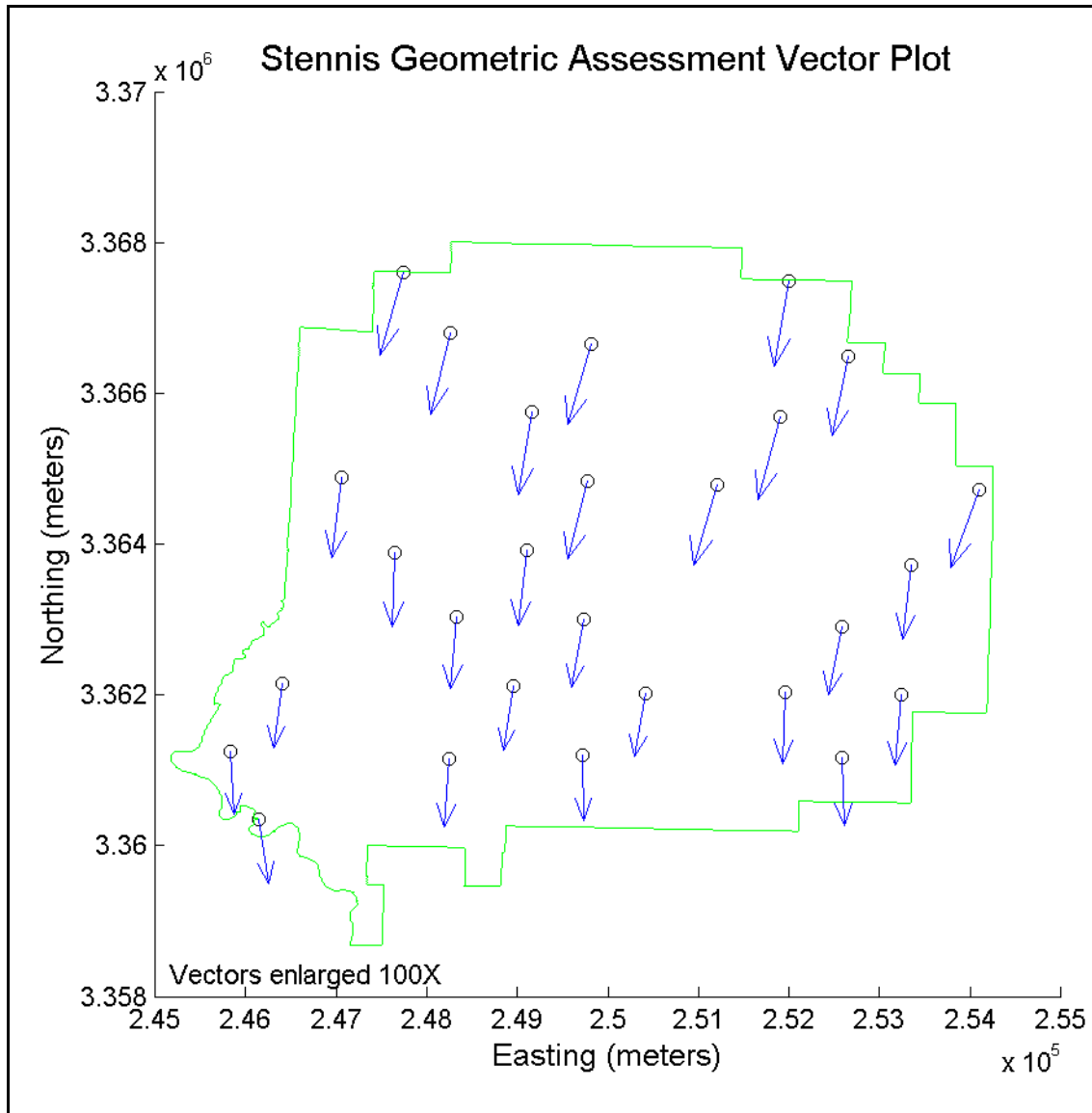


Figure C-3. Vector plot of target errors for acquisition on December 15, 2003.

Table C-7. Geopositional point-by-point computations, December 26, 2003.

Point	diff. in X (ΔX)	(ΔX^2)	diff. in Y (ΔY)	(ΔY^2)	magnitude horiz. diff. (ΔR)
1-A	2.87	8.23	-3.61	13.04	4.61
1-B	1.52	2.32	-3.30	10.90	3.64
1-C	1.96	3.83	-3.49	12.15	4.00
1-D	2.00	4.02	-3.60	12.92	4.12
1-E	2.23	4.99	-2.71	7.34	3.51
1-F	2.22	4.91	-3.43	11.78	4.09
1-G	2.34	5.47	-3.04	9.27	3.84
1-H	2.71	7.35	-3.39	11.48	4.34
1-I	2.93	8.58	-3.33	11.12	4.44
2-A	2.67	7.14	-3.81	14.48	4.65
2-B	1.89	3.58	-3.89	15.13	4.33
2-C	2.33	5.42	-4.18	17.47	4.79
2-D	2.15	4.64	-4.06	16.52	4.60
2-E	1.87	3.49	-4.06	16.50	4.47
2-I	2.60	6.74	-4.10	16.81	4.85
3-A	2.04	4.16	-3.75	14.06	4.27
3-C	3.06	9.38	-4.24	17.98	5.23
3-D	1.57	2.47	-3.96	15.71	4.26
3-E	1.95	3.79	-4.35	18.96	4.77
3-F	1.16	1.35	-5.23	27.34	5.36
3-G	1.60	2.56	-4.72	22.24	4.98
3-H	1.53	2.35	-3.92	15.34	4.21
4-C	1.93	3.72	-4.60	21.15	4.99
4-E	1.63	2.65	-4.48	20.04	4.76
4-G	2.15	4.63	-4.42	19.56	4.92
4-I	2.03	4.13	-4.36	19.03	4.81
5	1.63	2.66	-3.09	9.54	3.49
6	2.48	6.16	-3.25	10.59	4.09
7	2.23	4.99	-2.99	8.93	3.73
Note: All measurements are in meters.					

Table C-8. Geopositional accuracy results for acquisition on December 26, 2003.

Remote Sensing System		OrbView-3	
Acquisition Date	12/26/2003	Imagery Band	PAN
Number Targets Used			
<i>n</i>	29		
NSSDA requires 20 or more points.			
ΔX & ΔY			
Average ΔX	2.11 m	Average ΔY	-3.84 m
Standard Deviation ΔX	0.47 m	Standard Deviation ΔY	0.59 m
RMSE X	2.16 m	RMSE Y	3.88 m
Test for Departure from Circular Distribution		Root Mean Square Error Summary	
St. Dev. Min Max Ratio	0.80	RMSE _{net}	4.45 m
St. Dev. Min Max Ratio should be at least 0.6 for Circular Error assumptions.			
Bias & Random Error Estimates			
μ_H (Bias)	4.38 m	σ_C (Circular Standard Error)	0.53 m
μ_H/σ_C	8.28		
If μ_H/σ_C is greater than 0.1, then error calculations should account for bias.			
Circular Error			
CMAS (<i>CE</i> ₉₀)	6.49 m	Empirical <i>CE</i> ₉₀	4.98 m
NSSDA Accuracy _r (<i>CE</i> ₉₅)	7.40 m	Empirical <i>CE</i> ₉₅	5.24 m
NSSDA & CMAS assume bivariate normal distributions with zero bias.			
Note: The μ_H/σ_C value in this case (8.28) strongly indicates against characterizing this data with a zero bias assumption. CMAS and NSSDA Accuracy_r are included here for reference only. When these RMSE-based calculations have been applied to similar data at SSC, overestimation of 10-50% has been demonstrated.			

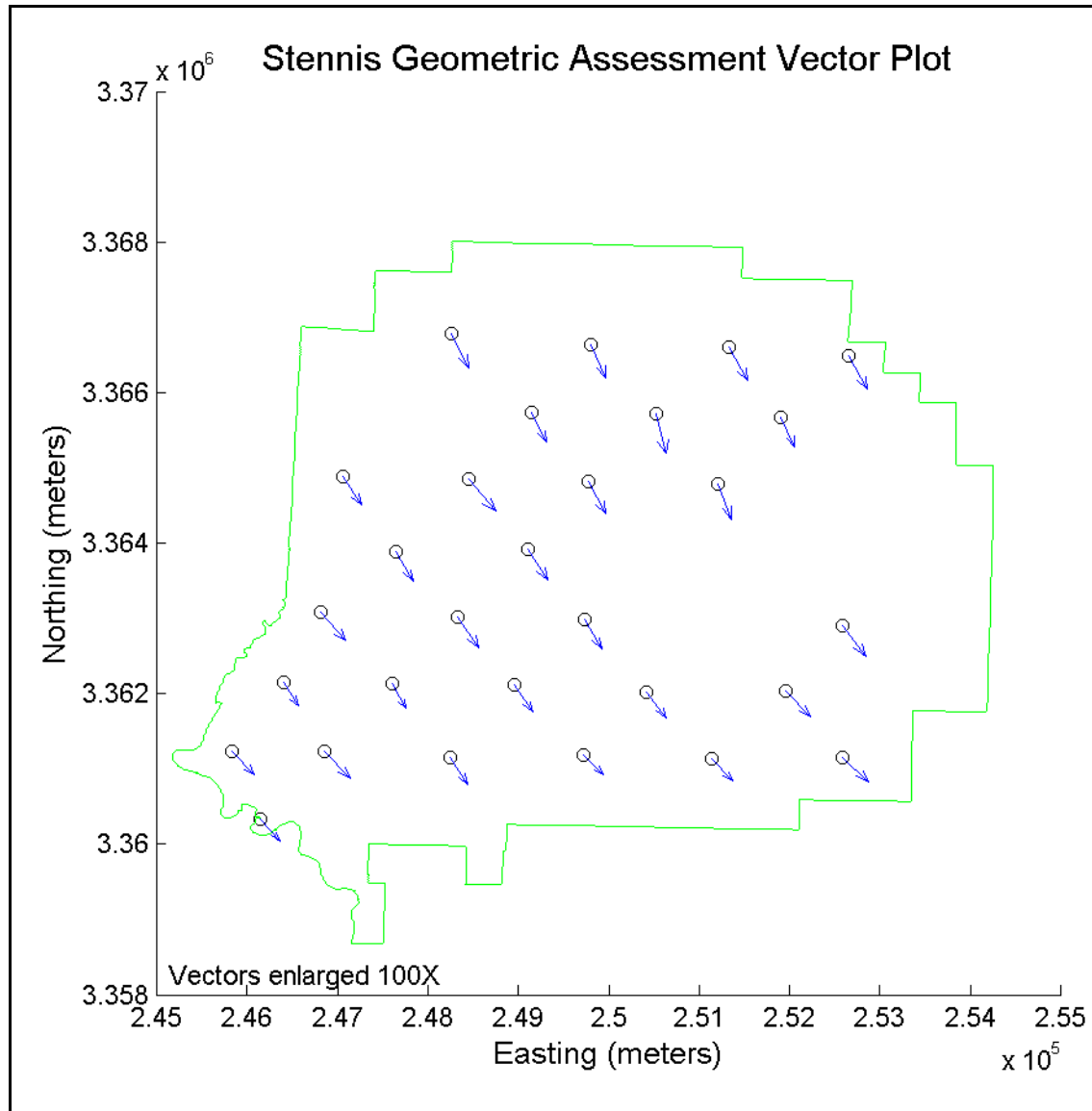


Figure C-4. Vector plot of target errors for acquisition on December 26, 2003.

Table C-9. Geopositional point-by-point computations, January 12, 2004.

Point	diff. in X (ΔX)	(ΔX^2)	diff. in Y (ΔY)	(ΔY^2)	magnitude horiz. diff. (ΔR)
1-C	-5.54	30.64	-0.94	0.89	5.61
1-D	-6.03	36.31	-1.19	1.43	6.14
1-E	-5.80	33.59	-0.63	0.39	5.83
1-F	-5.89	34.69	-0.92	0.85	5.96
1-G	-5.73	32.82	-1.09	1.19	5.83
1-H	-5.34	28.53	-1.43	2.03	5.53
1-I	-5.21	27.15	-1.31	1.71	5.37
1-J	-5.77	33.25	-1.47	2.17	5.95
2-C	-4.78	22.85	-1.38	1.90	4.97
2-D	-4.94	24.36	-1.04	1.08	5.04
2-E	-5.16	26.64	-0.96	0.91	5.25
2-F	-5.62	31.56	-1.35	1.83	5.78
2-G	-4.99	24.86	-1.50	2.24	5.21
2-I	-5.46	29.78	-1.11	1.23	5.57
2-J	-4.47	20.00	-1.00	1.01	4.58
3-A	-4.06	16.51	-1.50	2.26	4.33
3-B	-5.20	27.02	-1.87	3.51	5.53
3-D	-4.38	19.22	-1.92	3.70	4.79
3-E	-5.11	26.12	-1.28	1.65	5.27
3-F	-4.94	24.43	-2.19	4.79	5.41
3-G	-5.56	30.96	-1.75	3.06	5.83
3-H	-4.53	20.53	-1.92	3.70	4.92
4-B	-5.42	29.42	-1.88	3.52	5.74
4-C	-5.24	27.47	-1.61	2.60	5.48
4-D	-5.17	26.68	-2.54	6.43	5.75
4-E	-4.48	20.09	-2.47	6.09	5.12
4-H	-5.46	29.86	-2.27	5.17	5.92
4-I	-4.92	24.23	-1.59	2.52	5.17
5	-5.46	29.86	-1.06	1.12	5.57
6	-5.53	30.55	-1.20	1.44	5.66
7	-5.41	29.31	-1.48	2.20	5.61
Note: All measurements are in meters.					

Table C-10. Geopositional accuracy results for acquisition on January 12, 2004.

Remote Sensing System		OrbView-3	
Acquisition Date	1/12/2004	Imagery Band	PAN
Number Targets Used			
<i>n</i>	31		
NSSDA requires 20 or more points.			
ΔX & ΔY			
Average ΔX	-5.21 m	Average ΔY	-1.48 m
Standard Deviation ΔX	0.48 m	Standard Deviation ΔY	0.48 m
RMSE X	5.23 m	RMSE Y	1.55 m
Test for Departure from Circular Distribution		Root Mean Square Error Summary	
St. Dev. Min Max Ratio	0.99	RMSE _{net}	5.46 m
St. Dev. Min Max Ratio should be at least 0.6 for Circular Error assumptions.			
Bias & Random Error Estimates			
μ_H (Bias)	5.42 m	σ_C (Circular Standard Error)	0.48 m
μ_H/σ_C	11.37		
If μ_H/σ_C is greater than 0.1, then error calculations should account for bias.			
Circular Error			
CMAS (<i>CE</i> ₉₀)	7.28 m	Empirical <i>CE</i> ₉₀	5.93 m
NSSDA Accuracy _r (<i>CE</i> ₉₅)	8.30 m	Empirical <i>CE</i> ₉₅	5.96 m
NSSDA & CMAS assume bivariate normal distributions with zero bias.			
Note: The μ_H/σ_C value in this case (11.37) strongly indicates against characterizing this data with a zero bias assumption. CMAS and NSSDA Accuracy _r are included here for reference only. When these RMSE-based calculations have been applied to similar data at SSC, overestimation of 10-50% has been demonstrated.			

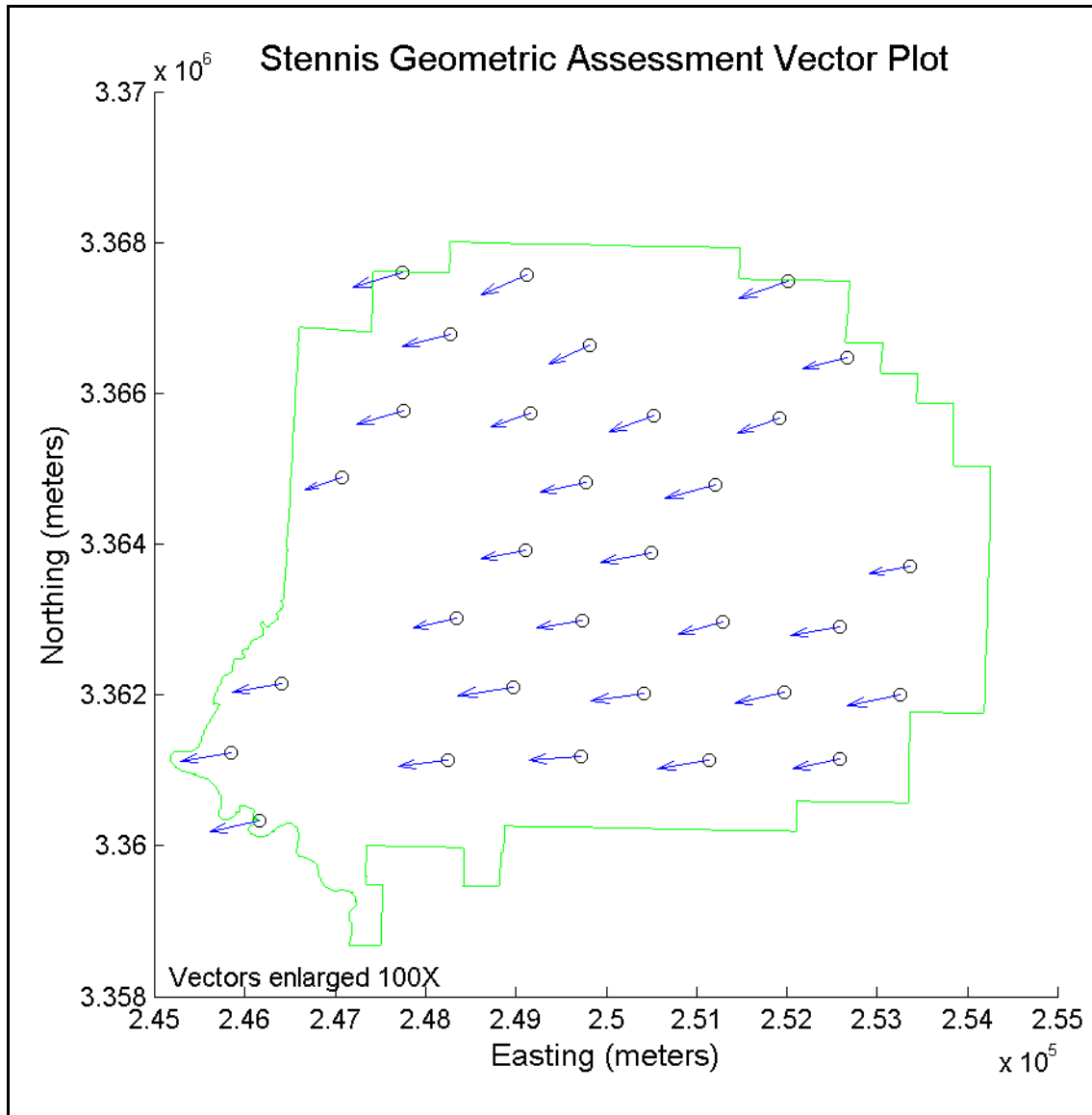


Figure C-5. Vector plot of target errors for acquisition on January 12, 2004.